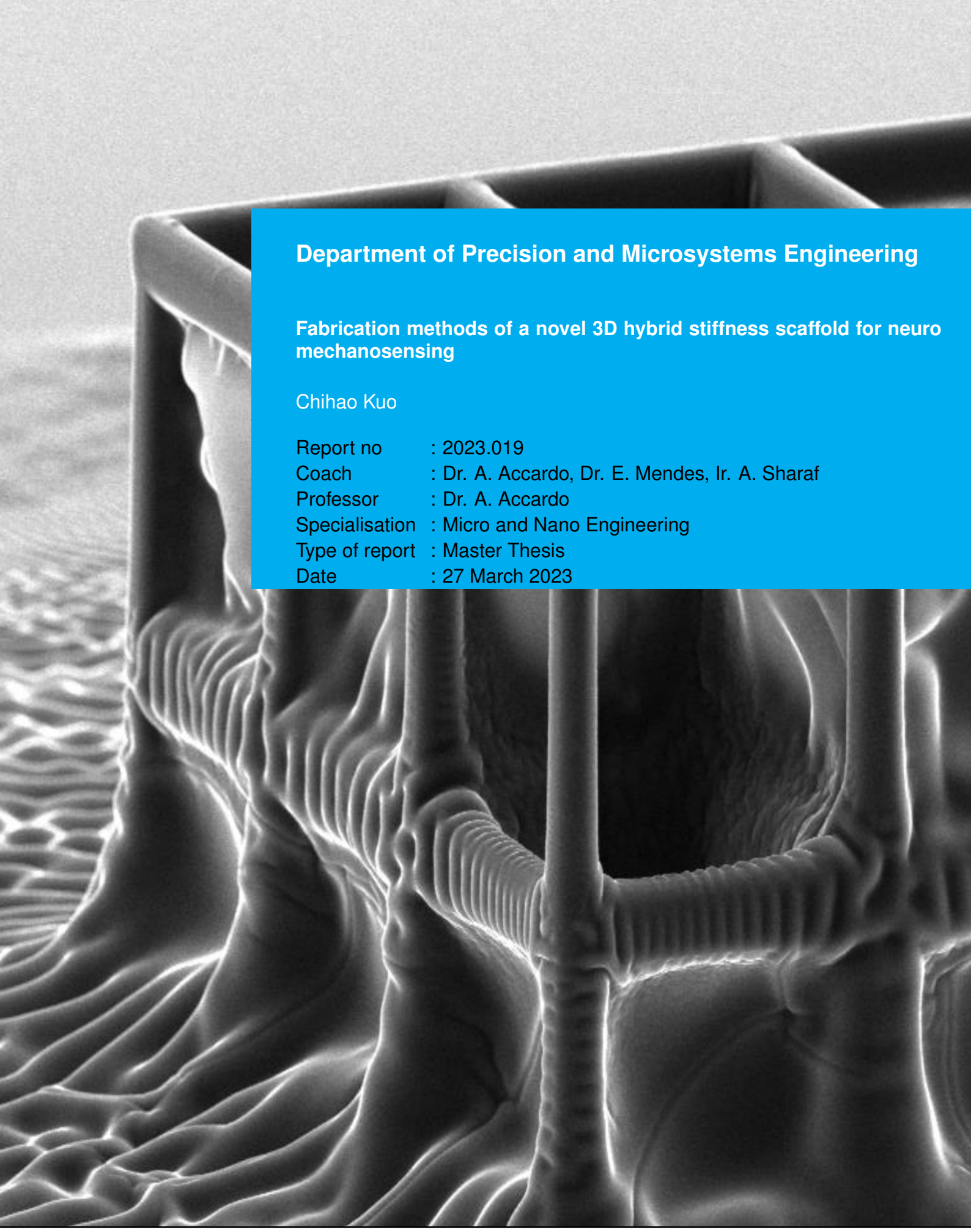

Department of Precision and Microsystems Engineering

Fabrication methods of a novel 3D hybrid stiffness scaffold for neuro mechanosensing

Chihao Kuo

Report no : 2023.019
Coach : Dr. A. Accardo, Dr. E. Mendes, Ir. A. Sharaf
Professor : Dr. A. Accardo
Specialisation : Micro and Nano Engineering
Type of report : Master Thesis
Date : 27 March 2023

TU Delft Delft University of Technology

Challenge the future

Delft University of Technology

ME56035 MSc Thesis

Master thesis

Fabrication methods of a novel 3D hybrid stiffness scaffold for neuron mechanosensing

Author:
Chihao Kuo (4585968)

Supervisors:
Dr. Angelo Accardo
Dr. Eduardo Mendes
Daily supervisor Ir. Ahmed Sharaf

March 27, 2023

TU Delft Delft University of Technology

MSc program Mechanical Engineering, Department of Precision and Microsystems Engineering

This thesis is confidential and can not be made public until 30/03/2025

An electronic version of this thesis is available at http://repository.tudelft.nl

Acknowledgement

I am very thankful to Dr. A. Accardo, Dr. E. Mendes and Mr. A. Sharaf for giving me the opportunity to dedicate my master thesis to a subject I am very much fascinated about. They have pushed me to work more efficiently and clearly in scientific research for which I am very grateful for.

I would like to express my thanks and gratitude to those who have helped me during my experiments. Mr. Z. Li who helped me with the Raman measurements and setup, Ms. A. Kooijman for performing the contact angle measurements. All the PME lab support staff and colleagues from the Nanoscribe group have also been very helpful to me during multiple stages of the thesis.

Abstract

In order to study neuronal cell behavior, the neurons are cultured on substrates in a lab and then experimented on. These substrates must feature a soft (Young's Modulus, E $\approx 1\,\text{kPa}$) and 3D structure to mimick the *in vivo* brain environment. A commonly used class of materials for this substrate is hydrogels. The conventional approach cultivating cells in petri dishes, although reproducible, inexpensive and easy to handle, involves 2D planar and stiff (E $\approx 1\,\text{GPa}$) substrates which are not reproducing the softness and the tri-dimensionality followed by the structure in our brain. This difference in substrate dimension results in different neuronal cell behavior as it has already been shown in literature.

Researchers have tried to circumvent this problem by manufacturing 3D scaffolds, mimicking the *in vivo* brain environment. Most 3D scaffolds are stiff, similar to the aforementioned petri dishes. A different material is therefore being used in research, a soft polymer called hydrogel. The hydrogel scaffolds matches the softness and the tri-dimensionality of our brain. However, due to the softness of the hydrogel (E = 1 $\sim$ 100 kPa) the scaffolds lack rigidity and tend to collapse on their own. This research attempts to design a manufacturing method for a hybrid stiffness scaffold solving the issue. This scaffold consists of a stiff polymeric base scaffold created via a 3D printing technique called two-photon polymerization. A layer of soft hydrogel is subsequently grown on the scaffold surface via a hydrogel crosslinking method called the surface-initiated method.

This paper shows that the base scaffold, made of IP-S resin from Nanoscribe, can be manufactured and displays high rigidity with an average Young's modulus of $E_{average} = 2.85\,\text{GPa} \pm 0.575\,\text{GPa}$. The hydrogel (PEGMA) used for this application shows similar softness as the brain environment with an average Young's modulus of $429.3\,\text{Pa} \pm 93.7\,\text{Pa}$. The surface-initiated method is shown to be a successful method for growing a soft hydrogel layer on flat structures. This method is also able to grow soft hydrogel on scaffolds with pores, but clogging of the pores appears.

Although high specificity of hydrogel coverage was not reached in this research, this paper can pave the way for a future hybrid stiffness scaffold used in neuronal cell culture research.

Contents

Chapter 1
Introduction

As part of a continuous search for a better understanding of the human brain, intensive research has led the field of tissue engineering to develop engineered micro-environments mimicking such tissue. The brain is one of the softest tissues found in humans (Young's modulus, E $\approx$ 1 kPa) [1, 2] and consists mostly of neurons, glial cells, and the brain extracellular matrix (bECM) [3].

Neuron culture has traditionally been performed in 2D petri dishes where the underlying substrates are made of polystyrene or glass [4]. These substrates are very stiff (E $\approx$ 3 - 50 GPa) [5, 6]and affect neuronal cells in different ways. Soft media like hydrogels have been found to promote neurite outgrowth and neural cell growth [7, 8, 9] and are thus more favorable than stiff media such as plastic and glass. The dimensionality of the substrate is also important. 2D substrates result in different outcomes than 3D ones, because in 2D cell cultures the substrate does not mimic the natural structures of brain tissue. As a result of this 2D substrate, the cell-cell and cell-ECM interactions are lost, which are vital for cell differentiation, migration, and proliferation [10].

Soft substrates similar to brain tissue are thus needed in order to support neuron growth. A possible material for this application is hydrogel. Hydrogels have excellent properties similar to bECM: typical hydrogels have a Young's modulus around the same order of magnitude (E $\approx$ 10 $\sim$ 100 kPa) [11] and are biocompatible. This is because they consist of crosslinked polymeric networks that have the ability to swell upon absorbing water.

The logical scenario would be to use scaffolds purely made of hydrogels. An additive manufacturing (AM) method, often called 3D-printing, must be able to reproduce the micrometric resolution needed to make microstructures close to the cell size. The material used in this 3D-printing method must also be a hydrogel to match the stiffness of brain tissue. The 3D matrices need to have high porosity and pore sizes that are up to thrice as big as the cell body (20 µm) of the neuron [12] to support cell colonization in all directions (lateral and vertical). These conditions stimulate cell proliferation, adhesion, and migration which are essential for *in vitro* cell culture studies [13]. Two photon polymerization (2PP) is a very promising 3D printing technique for feature sizes down to a submicron level, able to match the size of neurons. So far, successful reports have been made on creating micrometric hydrogel scaffolds for cell culture studies with the use of 2PP already [14, 15]. However, pure hydrogel scaffolds made with 2PP are fragile and prone to collapse. We propose therefore another approach by designing a stiff (E $\approx$ 5 GPa) polymeric scaffold using 2PP and coat the same scaffold with a micrometric soft (E $\approx$ 100 kPa) layer of hydrogel to mimick the same bECM conditions in the brain. A hydrogel layer of a few micrometers on the scaffold could be sufficient to trick the neurons into acting similarly *in vitro* as *in vivo*.

To the best of the author's knowledge, there are no reports of attempting the fabrication of a **stiff 3D scaffold** using 2PP with microscale resolution and subsequently coating it with a **controllable soft micrometric layer** of hydrogel. This thesis will dive deeper into a developed coating mechanism and explore the possibilities and limits of this mechanism in conjunction with 2PP.

Chapter 2
Review of Literature Survey

In light of the rapidly advancing research on neuron cell culture methods, a proper understanding of neuron mechanobiology, hydrogel chemistry, and 3D printing techniques is necessary in order to fully understand this thesis. This chapter will revise what has been discovered during the literature survey and summarize the information needed to understand the problem statement and possible solutions.

2.1 Neural cell (mechano)biology

2.1.1 The Brain Extracellular Matrix

Neurons in the brain reside in a medium called the (brain) extracellular matrix, (b)ECM. It consists of two parts, the basement membranes and the connective tissues. Basement membranes and connective tissues form a network of strings in which neurons can adhere to. The first one is usually found next to blood vessels in the brain and consist mostly of (type IV) collagen fibers [16], while the latter fills up the rest of the space and consist of proteins like proteoglycans. The collagen fibers resist tensile forces while proteoglycans form a gel-like network and resist compressive forces [17]. The long proteoglycan strings contain side chains, glycosaminoglycans, which are sugars. These sugars in the bECM can retain water which in turn causes the bECM to be soft.

The ECM is a complex environment providing many different cues to neurons which can sense and react to accordingly [18]. The different cues that the ECM provide can be classified as chemical, geometrical or mechanical. Chemical cues provided by proteins and soluble macromolecules. Geometrical and mechanical cues include pore sizes, porosity, topography, geometry, and stiffness [18]. For example, Hanson Shepherd et al. demonstrated that for neurons with a soma of $\sim 10\,\mu m$ the optimal pore size for cell migration (lateral and vertical direction) is found to be around thrice as big as the soma [12].

The brain ECM has an average Young's modulus of 1 kPa, which makes it the softest tissue found in the human body [19].

Other types of cells like microglia, glial cells and brain microvascular cells are also present in the brain and are important for neurons to function, but are beyond the focus of this thesis.

2.1.2 2D and 3D Cell Environments

Literature has shown the impact that 2D and 3D environments can have on neuronal cell development. Many important aspects of cell development are lost in 2D, such as cell-cell and cell-matrix interactions, cell polarity, and cell morphology [10]. These interactions are responsible for cell differentiation, proliferation, and other cellular functions [20], while a changed morphology can affect their function [21] and cell signaling [22].

On the other hand, a 3D environment boosts synaptic activity in neural networks [23] and also promotes neural migration [24]. Other papers found more neuritic extensions in a 3D environment than in a 2D layered one [25]. Figure 2.1 Laplaca et al. shows the difference of a neuron's morphology when cultured in 2D and in 3D. In 2D, the neuron is more flat and shows less neurite outgrowth as opposed to 3D culture [26].

2D culture models are thus associated with numerous problems previously mentioned, while 3D models appear to be a good alternative.

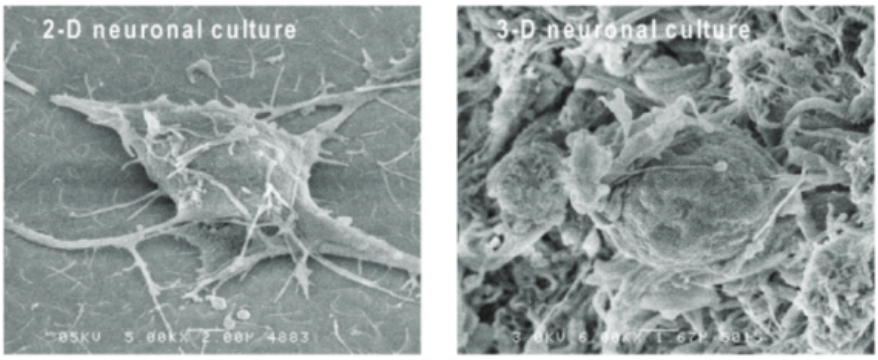

Figure 2.1: Left: Neuronal cell culture in 2D shows flat morphology of a neuron and poor neuritic outgrowth. Right: Neuronal cell culture in 3D shows round morphology of a neuron and abundant neuritic outgrowth by Laplaca et al. [26]

2.1.3 Mechanosensing

Besides the geometric differences of 2D and 3D environments in the context of neuronal cell developments, the stiffness of the surroundings is another important aspect which can influence neuronal growth.

Mechanosensing describes the cell's ability to sense the physical cues of its surrounding environment such as forces, strain, topographies, and stiffness. Cell differentiation, migration, proliferation, and adhesion all greatly depend on mechanosensing [27]. Neurons sense through complexes called lamellipodia and filopodia for migration and differentiation purposes [28]. These are located in areas found at the edge of the soma (cell body) during differentiation and migration [29] or at the tip of axons and dendrites and are part of the so-called growth cones, during neurite outgrowth [30]. Filopodia are pointy and contain bundled F-actin filaments due to a process named F-actin polymerization,

which makes the cell crawl [31]. Lamellipodia are more spread out and do not contain bundled F-actin. These complexes sense a variety of "attractive" and "repulsive" cues in the ECM [32] via focal adhesions or focal spots. They contain integrins which are glycoproteins that directly binds the cell cytoskeleton to the ECM. These integrins are receptors which can trigger signaling cascades inside the cell when bound to a ligand. This kind of sensing happens chemically, but some can also respond to physical ECM properties such as traction forces from the bECM [33]

2.2 Chemistry

2.2.1 Free Radical Polymerization

Free radical polymerization (FRP) is at the heart of this thesis, so the basic principle is reviewed here. FRP is a chemical reaction where two ends of a molecule are covalently bound via crosslinking. This covalent bonding is called chemical crosslinking, and is mechanically and thermally stable. Crosslinking in FRP happens when a crosslink reagent is activated and initiates the polymerization, called a thermo-initiator if initiated via heat or photo-initiator via irradiation.

The activated initiators are radicals and are very reactive. They will undergo reactions with special bonds from functionalized groups in a molecule. In FRP, these special bonds are double-bonded carbon atoms which can be found in two different functionalized groups; allyl- and vinyl-groups.

Out of these two functionalized groups, the vinyl-groups are often used for FRP because the radical vinyl-groups are more unstable and thus very reactive, while also less likely to terminate via self-stabilization or hydrogen abstraction [34]. Vinyl-groups will therefore result in faster polymerization process and high molecular weight polymers than allyl-groups [35]. This indirectly also means that vinyl-groups require less (toxic) initiators as well in order to work effectively.

Crosslinking and polymerization starts when these radicals "attack" the special bonds, breaking the double-bonded carbon atoms and freeing up space by transferring the radical energy onto the monomer. This monomer becomes a radical itself and will propagate the chain-reaction by reacting with other monomers (Fig 2.2). The polymerization usually terminates when a growing chain reacts with another growing chain.

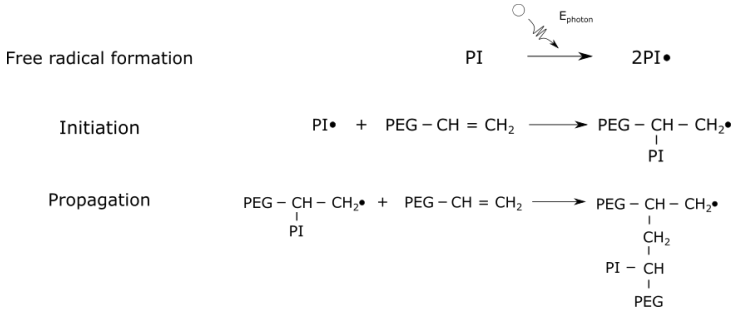

Figure 2.2: Free radical polymerization steps. First it starts with the formation of a radical which is triggered under UV light. The free radical subsequently reacts with a monomer, transferring the energy, and initiates the polymerization. This process will continue (propagation) with other monomers.

2.2.2 Hydrogels

Hydrogels are polymers which are crosslinked to form a network, where hydrophilic (side)chains and pockets of space allow the polymer retain large amounts of water. This property makes hydrogels very soft, with a Young's modulus ranging from 1-100 kPa. Further, hydrogels are bio-compatible, thus ideal for biological research. For neuron cell culture purposes, hydrogels have been employed and researched because they can match the stiffness of soft tissue of the brain ECM, as opposed to other common materials such as PDMS (Young's modulus $\sim$ 1 - 3.5 MPa) [36], or more commonly, polystyrene (3 GPa) and glass (50 GPa) [5, 6].

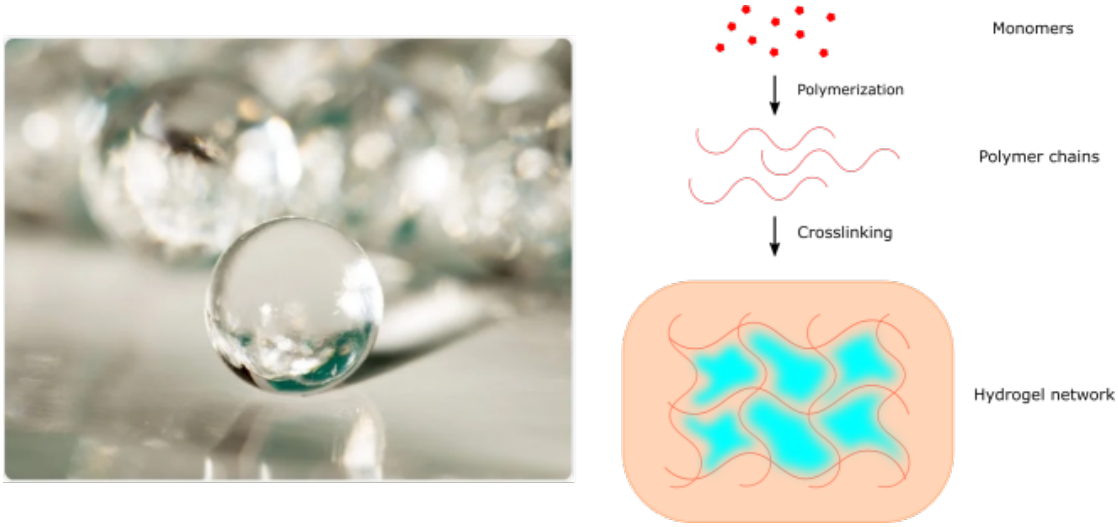

Figure 2.3: Hydrogel forming steps from its building blocks to a network through polymerization and crosslinking. The hydrogel monomers start by forming long polymer chains, which will crosslink with each other and create a network where water can be stored.

Hydrogels were classified according to its derivation. The classifications of hydrogels were natural hydrogels and synthetic hydrogels. Natural hydrogels can be derived from

nature while synthetic hydrogels are only produced in labs [37]. Natural hydrogels are advantageous because they are easily biodegradable. They also contain (fibrous matrix) proteins and proteoglycans which are the main components of the ECM in tissues [38, 39]. Natural hydrogels have also been proven to be an exceptional substrate for neuron growth. Matyash et al. managed to make an alginate hydrogel substrate, naturally found in brown algae, through ionic crosslinking and successfully cultured human and rat neurons showing neurite growth [40]. Lengths between 40 to 50 µm per 1000 μm^2 of neurite outgrowth were measured on the alginate hydrogels (E = 20.8 kPa) after culturing for six days. This was double the length of neurons cultured on polystyrene coated with Poly-L-lysine (PLL). On top of that, MAP2 and β-tubulin III, which are associated with microtubuli formation in dendrites [41] and axons [42] respectively, were expressed by the neurons grown on the alginate hydrogel.

Natural hydrogels have beneficial traits for cellular processes and thus seem like the obvious choice to use as a substrate for cell culture. However, as more research is being done, new synthetic hydrogel materials are being developed gradually replacing the natural ones. This is because synthetic hydrogels have a higher water absorption ability, longer shelf life, and their raw materials are easier to make rather than trying to use a natural source to extract them from [43]. Synthetic hydrogels are therefore also easier to reproduce. On the other hand, synthetic hydrogels although exhibiting excellent biocompatibility, lack any ligands for promoting cell adhesion and migration (laminin, collagen I/II, fibronectin) [44] which can be found instead in natural hydrogels.

Hydrogel synthesis involves physical and chemical crosslinking. Physical crosslinking includes hydrogen bonding (H-bonding), ionic bonding, and physical entanglement of polymer chains. Chemical crosslinking involves homogeneous covalent bonds and is stronger than the weaker forces associated with physical crosslinking [45]. The mechanical properties of physically crosslinked hydrogels are poor compared to their chemical counterparts because the physical interactions are reversible whereas covalent bonds taking place in chemical crosslinking is irreversible [46]. For strong and stable hydrogels, one should thus employ chemically crosslinking.

In order for hydrogel monomers to go through FRP, functional groups containing double-bound carbon atoms must be present. If this is not the case it can be enabled by functionalizing the monomers. Functionalizing is the process where new functions and properties are added to a chemical compound. In our case, vinyl groups (CH_2=CHR) or allyl groups (CH_2=$CHCH_2$R) are added onto the polymer chain [47], "functionalizing" the monomer.

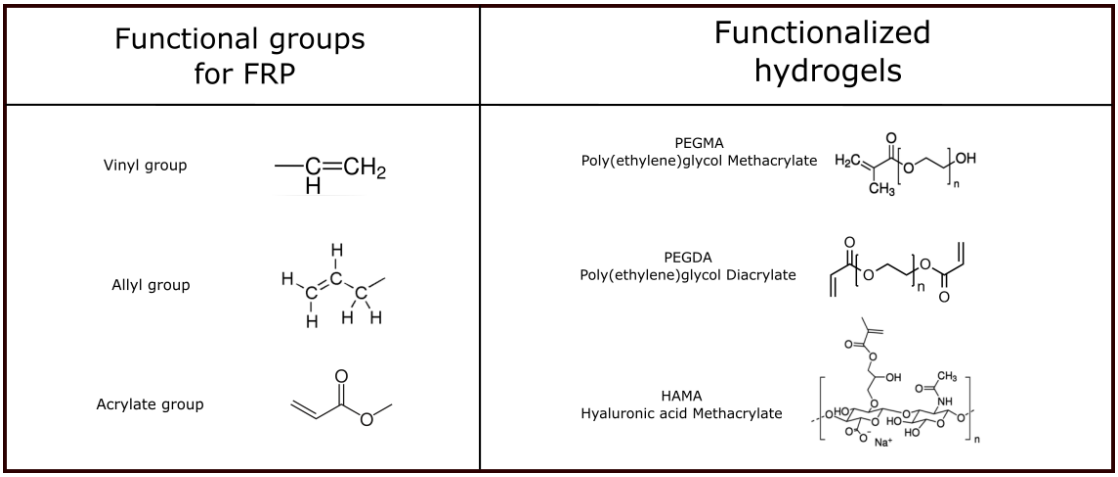

Figure 2.4: Functional groups and examples of functionalized hydrogel monomers for FRP

2.2.3 Coating Method Strategies

During the literature survey, many different coating methods were investigated and categorized on the growth mechanism. The mechanisms were a "grafting to" technique and a "grafting from" technique. The "grafting to" technique refers to anchoring polymerized hydrogel chains onto a sample surface while the "'grafting from" one means that the hydrogel polymer chains grow from the sample surface (see Fig. 2.5). Two techniques to apply hydrogel layers on top of other materials, which stood out from the survey, were a condensation-reaction based method [48] and a surface-initiated based method [49].

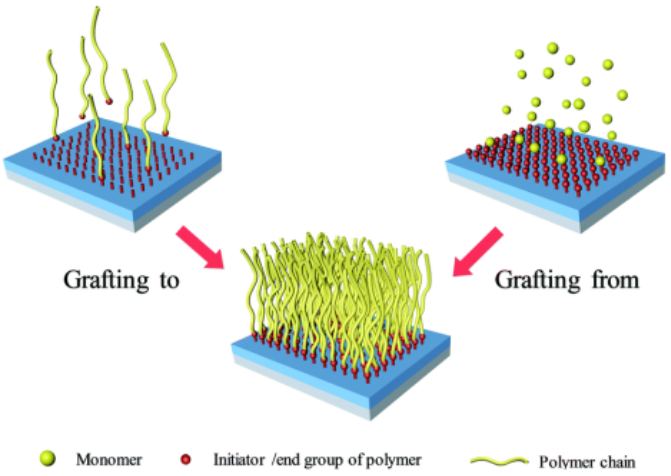

Figure 2.5: "Grafting to" vs "Grafting from" techniques [50]

The condensation reaction method falls under the "grafting to" category. A conventional method to apply a hydrogel layer onto a substrate is by polymerizing, crosslinking, and interlinking the hydrogel monomers all at once under UV light. Yao et al. decoupled this process by first co-polymerizing the hydrogel monomers into long polymer chains, then, via condensation reactions, they crosslinked and interlinked the polymer chains with each other and on the substrate surface (Fig 2.6).

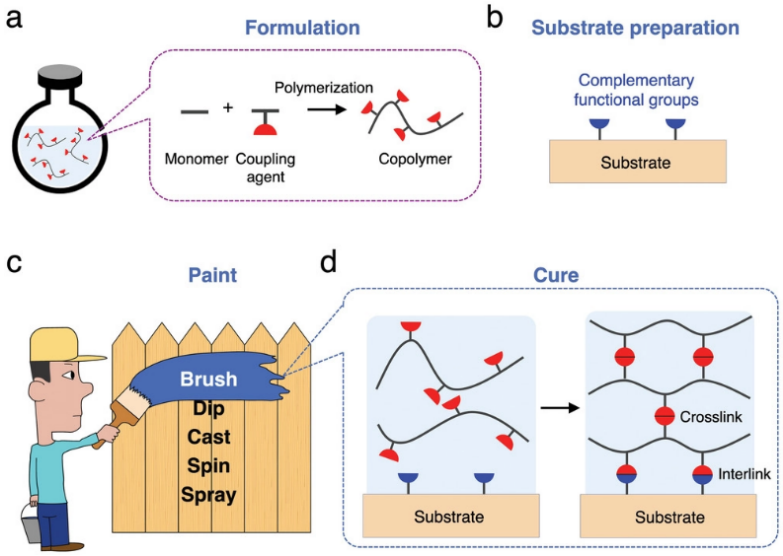

Figure 2.6: Principle of hydrogel paint of Yao et al. [48] a) Formulation: monomer units and coupling agents copolymerize into polymer chains, but do not crosslink into a network, resulting in an aqueous solution. The solution may also contain other compounds for various functions but are not drawn here. b) Substrate preparation: functional groups complementary to the coupling agents are imparted onto the surface of a substrate. c) Paint: The aqueous solution is painted on the substrate by various operations. d) Cure: The coupling agents react with each other to crosslink the polymer chains into network and react with the complementary functional groups to interlink the polymer network to the substrate

Condensation reactions join two molecules together where water molecules (or other small molecules) get released (Fig 2.7.1). This can happen between two hydroxy groups. Yao et al. first co-polymerized MAPTMS with acrylamide (AAm) via FRP to form long MAPTMS-*co*-AAM uncrosslinked chains as a hydrogel precursor solution. Chain transfer agents (CTA) are present to prevent the polymer chain from polymerizing continuously. The viscosity of this precursor solution can be changed by changing the concentration of the MAPTMS or CTA before copolymerizing; the higher the concentration of MAPTMS, the higher the viscosity while the inverse is true for CTA concentrations. The hydrogel precursor can then be applied differently on the samples, e.g. via dip-coating, spinning or spraying. Subsequently, the precursor will be cured in an oven. Their results showed a hydrogel layer ranging between 2 and 20 µm, depending on the viscosity of the hydrogel precursor solution, on metallic wires of 310 µm in diameter (see Fig. 2.8).

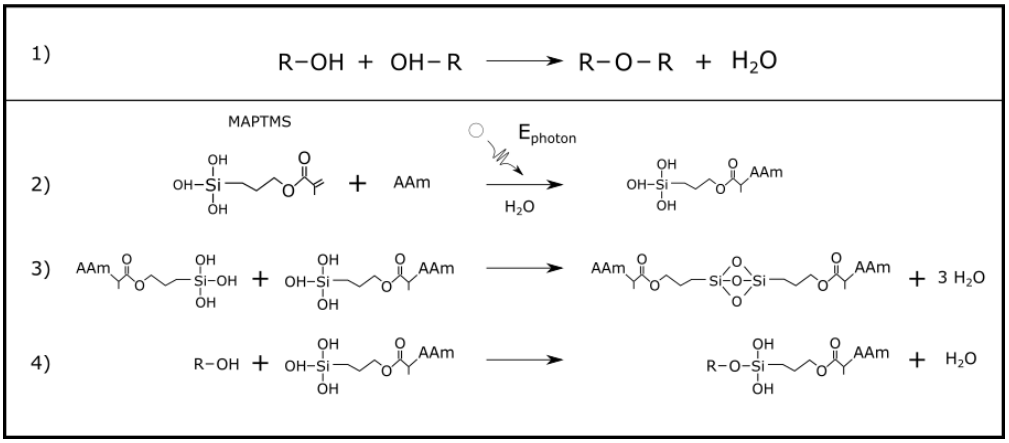

Figure 2.7: Condensation mechanisms 1) Generic condensation reaction between two hydroxy groups; Reaction mechanism of Yao et al.[48] 2) Copolymerization of MAPTMS and acrylamide (AAm) under UV light in aqueous solution into MAPTMS-*co*-AAm chains 3) Crosslinking between polymer chains via condensation reaction between silanol groups to form siloxane bonds 4) Anchoring of polymer chains onto a surface with hydroxy groups via condensation reaction

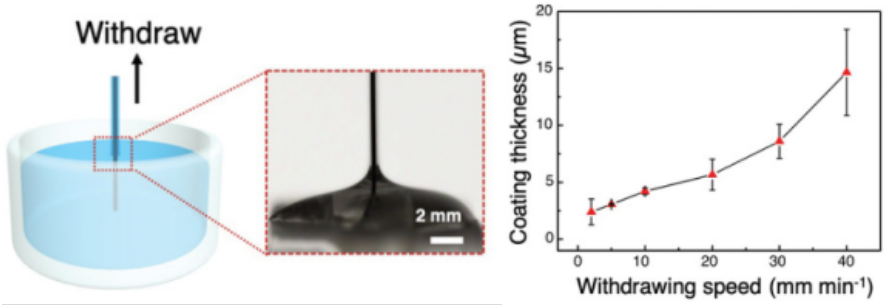

Figure 2.8: Nitinol wires were dipcoated in the MAPTMS-*co*-AAM hydrogel precursor with different speeds, resulting in varying thicknesses of hydrogel layers depending on the speed [48].

The other technique that stood out from the literature survey was based on surface-initiation, a form of "grafting from" method. Here, Yu et al. [49] developed a different method by essentially "growing" hydrogel layers on top of substrates (Fig 2.9). They achieved this by first submerging their polymeric samples in organic solvents mixed with hydrophobic photo-initiators. The initiators seep into the polymer surface via swelling-driven surface absorption and create a surface-bound diffusion layer. After the first photo-initiator bath, the samples are placed in an aqueous hydrogel precursor solution containing hydrogel monomers and hydrophilic photo-initiators. The hydrophobic initiators act as grafting agents where hydrogel polymer chains will grow, while the hydrophilic initiators will polymerize the hydrogel monomer within and above the surface-bound diffusion layer. The hydrophobic initiators will not diffuse into the aqueous precursor solution and limits the polymerization to only the diffusion layer. The thickness of their hydrogel layer ranges from 10 to 25 µm and grew hydrogel on samples down to 50 mm in

size (see Fig. 2.10).

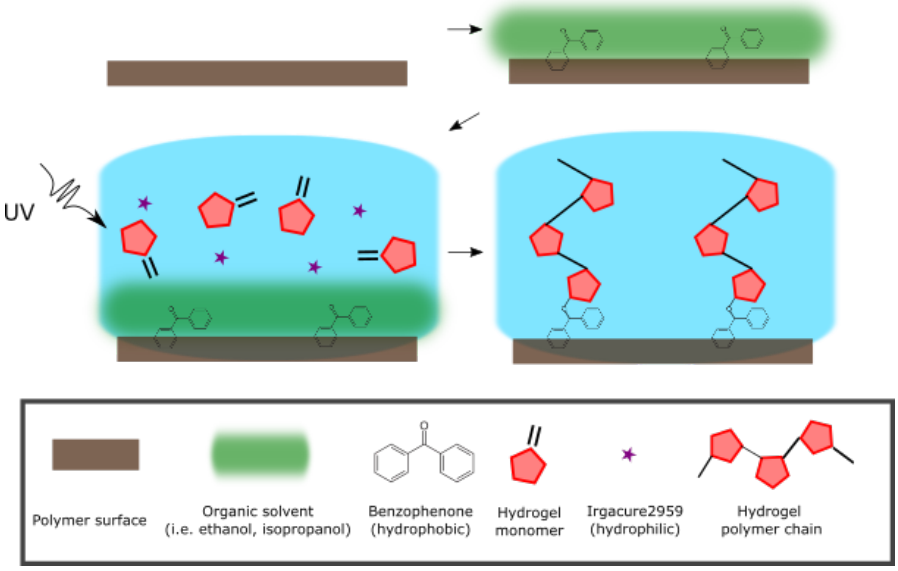

Figure 2.9: Schematic coating method of Yu et al.[49]. A plain polymer surface is first submerged in an organic solvent with hydrophobic initiators, creating a surface-bound diffusion layer at the polymer surface. Afterwards, the sample is polymerized in an aqueous hydrogel precursor under UV light, growing a hydrogel layer on top of the sample.

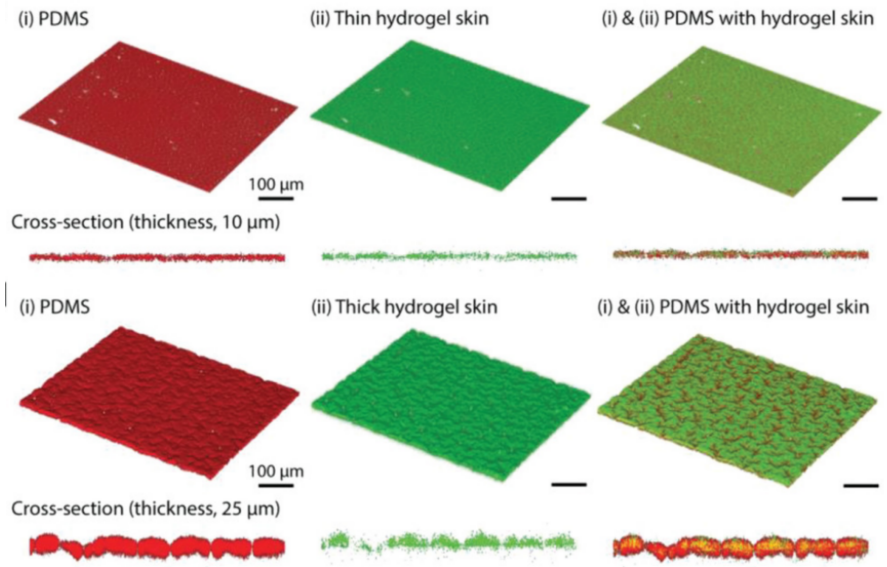

Figure 2.10: Confocal microscope images of thin (upper row) and thick (lower row) hydrogel skins on the PDMS substrates to illustrate the uniformity and tunable thickness of hydrogel skins. PDMS and hydrogel skins are colorized by Nile red and fluorescein, respectively. Different thicknesses were measured ranging from 10 to 25 µm [49].

2.3 Two Photon Polymerization

During the literature survey, different additive manufacturing techniques have been explored for 3D printing scaffold, such as bio-printing and digital light projection, and it was concluded that two-photon polymerization (2PP) is the best option for this project, as it enables the highest resolution prints while also being able to 3D print complex structures without the need of sacrificial supports.

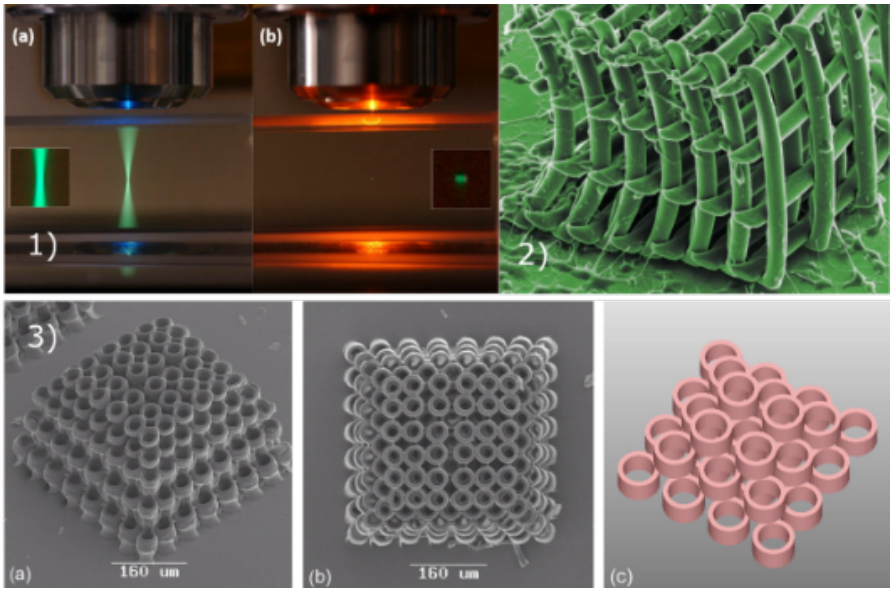

Figure 2.11: 1) One photon absorption range vs two photon absorption range (courtesy of S. Ruzin and H. Aaron, UC Berkeley) 2) 3D PEGDA hydrogel scaffold made via 2PP by Accardo et al. [15] 3) 3D PEGDA hydrogel scaffold made via 2PP by Ovsianikov et al. [14]

2PP in the context of cell mechanobiology is a subject which has been increasingly used in research only in recent years. This 3D printing technique has allowed researchers to study different aspects of cellular processes and its interactions with 3D structures obtained with 2PP.

For example, 2PP has been used in single-cell force measurements [51], to study cell interactions on patterned topographies [52], and microstructures [15] where high-resolution 3D printing is needed.

Typical materials employed in 2PP in cell mechanobiology are hydrogels because of their biocompatibility and are able to be polymerized via FRP in presence of a photoinitator.

The latter forms the focus of the thesis. Research has been done on creating (complex) 3D scaffolds via 2PP. Accardo et al. (Fig. 2.11.2) printed free standing 3D hydrogel made of PEGDA for neuron cell culture purposes. They showed neuritic extensions between 10 and 60 µm while the neurons formed a ramified network. Ovsianikov et al. (Fig.2.11.3)

created a 3D scaffold consisting of hollow cylinders with radius of 25 µm and lateral resolution of 200 nm [14]. This hydrogel scaffold was also made with PEGDA hydrogel.

Chapter 3
Research Design

3.1 Problem Statement

Current neuronal cell studies are trying to transition from a 2D to a 3D environment because a 3D scaffold represent the bECM more accurately than their counterparts [53]. The 3D environments are called scaffolds and are based on various materials made via the 2PP method. However, in order to accurately mimick the scaffolds properties *in vitro* with *in vivo*, many materials are not suitable. The major issue is the mismatch in stiffnesses of brain tissue and the scaffold material, where brain tissue Young's moduli are typically at 1 kPa while scaffold materials have typically Young's moduli of 1 GPa. To overcome this problem, researchers combine the high resolution ($< 1\,\mu m$) of the 2PP 3D printing technique with the low Young's modulus ($E \approx 100\,kPa$) and biocompatibility property of the hydrogel, resulting in pure hydrogel scaffolds. The fabrication of pure hydrogel scaffolds on a microscale is however difficult to realize with 2PP as the resulting scaffolds are fragile because of the low Young's modulus. Here, we propose a potential solution to this problem by developing a hybrid stiffness scaffold. A stiff base scaffold is 3D printed and subsequently coated with a soft hydrogel layer. This new hybrid stiffness scaffold could be the solution to the fragile pure hydrogel scaffolds which are being researched now. The new scaffold with adequate hydrogel layer thickness might be sufficient to mimick brain tissue *in vivo* and set the standard for future neuronal cell culture studies.

3.2 Research Question

The next research question is identified in order to find an answer for the problem statement:

"Which growth method can be used to enable the fabrication of a 3D complex stiff micrometric structure featuring a tunable micrometric layer of soft hydrogel?"

Sub questions were used to guide the project by highlighting the relevant topics:

1. Which materials and geometries can be employed for the 2PP printing of the 3D scaffold?
2. Which hydrogel(s) can be employed for coating the 3D scaffold?
3. Which growth methods enable the formation of micrometric hydrogel layers on the 3D scaffold?
4. Are the coatings uniform everywhere?
5. Is it possible to adjust the thickness of the hydrogel layer?

3.3 Research Approach

Two different methods have been proposed, one from Yu et al. [49] named surface-initiated photografting and one from Yao et al. [48] named dip-coating. Yu et al. demonstrated a method where the samples were coated with *hydrophobic* photoinitiators in organic solvent baths. Afterwards, the samples were crosslinked in a hydrogel precursor solution with *hydrophilic* photoinitiators under UV light. Yao et al. showed a different approach by playing with the viscosity of the hydrogel precursor solution by changing the MAPTMS concentration.

However, due to a combination of time-constraints and the many parameters that can be tuned in each of these methods, as well as the expected hydrogel layer should be adequate and controllable, we only adapted the surface-initiated methodology of Yu et al. to our scaffolds, because they showed more stable results with hydrogel thicknesses between 10 µm and 25 µm as opposed to the method of Yao et al., where layers of 2 µm to 20 µm where obtained, but heavily dependent on the speed of the dip-coating method.

First, the main 3D structures are designed and fabricated. Here, the most optimal printing parameters are tested and characterized on pedestals via SEM images, compression testing, and contact angle measurements. Then the hydrogel precursor will be prepared and the surface-initiated method will be tested on pedestals, characterized and evaluated. If sufficient, unit cells will be tested and the same characterization is performed. If it is also sufficient then the process will be performed on scaffolds. During the project, anytime when the results are insufficient, the same step will be reiterated with adjusted parameters until it is sufficient.

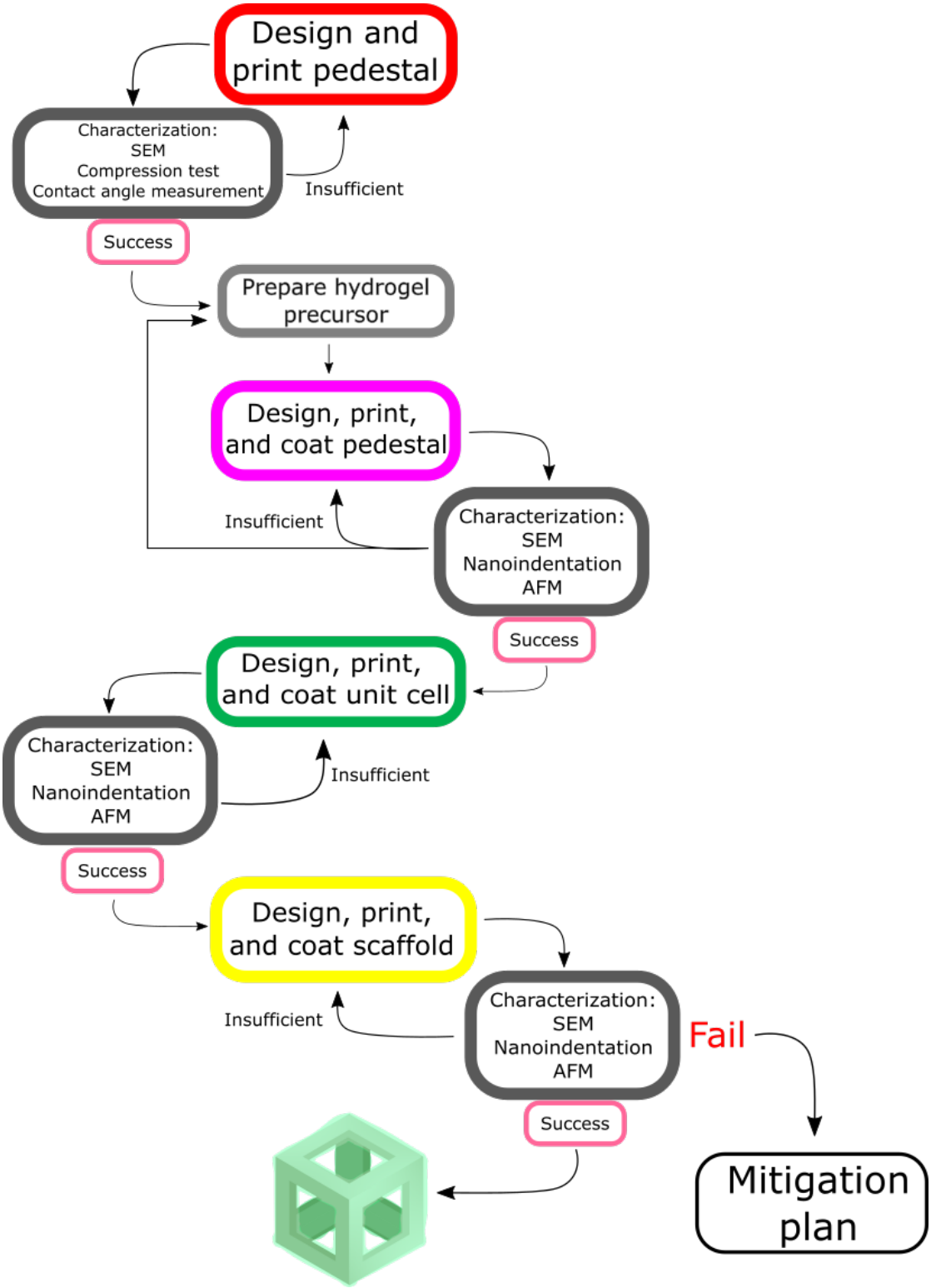

Figure 3.1: Project flowchart

Chapter 4
Methodology

4.1 Experimentation

4.1.1 Materials

Here is a list of materials and tools which have been used throughout the experimentation phase.

Chemicals:

- Aceton
- Benzophenone (BP)
- Ethanol
- Isopropanol (IPA)
- Irgacure184 (I184)
- Lithium phenyl-2,4,6-trimethylbenzoylphosphinate (LAP)
- Poly(ethylene)glycol-Methacrylate (PEGMA)
- Propylene glycol methyl ether acetate (PGMEA)
- 3-(Trimethoxysilyl)propyl methacrylate (MAPTMS)

Tools:

- SEM
- Raman
- Contact angle
- UV light
- Nanoscribe
- Magnetic mixer
- Femtotools
- AFM
- Nanoindenter
- Oxygen plasma cleaner
- UV oven (Photopol light curing unit from DentalFarm

- Spincoater
- Dessicator

Other:

- (soda lime) glass substrates
- 1.5 mL pipettes

4.1.2 Two Photon Polymerization

As mentioned in Section 3.3 Research Approach, the first phase is about the design and fabrication of the 3D microstructures. The Nanoscribe Photonic Professional GT2 printer is the 3D printer used for this occasion, utilizing the two-photon polymerization process.

2PP is a light-induced polymerization reaction, which is a method to initiate FRP. 2PP is initiated not just by any light source, but by a focused pulsating infrared laser shone into a photoresin containing monomers and photo-initiators. Usually for FRP to start, a single photon energy from UV light ($\lambda = \sim 380\,\text{nm}$) is needed to "activate" a photo-initator, but since 2PP uses near-infrared (NIR) light ($\lambda = \sim 760\,\text{nm}$) this does not happen immediately. Instead, the pulsating property of the laser allows the photo-initator to absorb two photon energy of lower energy at once, but only at the focal point of the laser where the light pulses come together. The energy of a (nearly) simultaneous absorption of two photons from NIR light is equivalent to one single photon from UV light, thus starting the FRP reaction. This property allows 2PP to create small oval-like volumes of polymerization called voxels. These voxels can reach sizes down to submicron levels ($\sim 100\,\text{nm}$), ideal for creating micro-metric sized scaffolds.

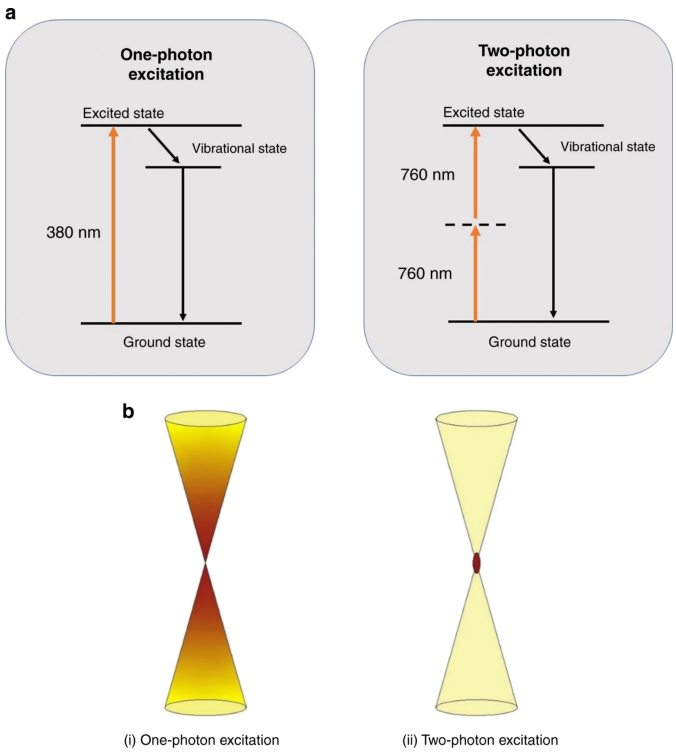

Figure 4.1: a) Comparison of the absorption energy of a single photon by UV light and two photons by near-infrared light. b) Schematic picture comparing the excitation volume of one-photon excitation (i) and two-photon excitation (ii). In 2PP, regions outside the laser focus are less likely to exceed the polymerization threshold of the photoresist [54].

Prior to the actual printing, substrate silanization is performed to improve the adhesion of the prints on the substrate. Glass substrates are first wiped clean with aceton, followed by IPA. After wiping, the substrates are activated with oxygen plasma for 10 min and immediately dipped in a solution of 0.2 % v/v MAPTMS in 30 mL of ethanol. Generally, 1 hour of silanization is sufficient given the microscopic size of the prints. MAPTMS functionalizes the substrate surface with silane (SiH_4) which acts as a coupling agent between the IP-S resin and the glass. The more time it silanizes, the better the adhesion. Silanization also improves the interface finding of the Nanoscribe which results in less failed prints. After printing, the unexposed resin is dissolved by submerging the samples in PGMEA for 25 minutes followed by IPA for 5 minutes and gently blow dried. The samples are stored in the Nanoscribe room at PME.

The polymer resin used for 3D printing is called IP-S, additional information and properties for this polymer can be found in Appendix A. The substrates are 25 mm x 25 mm x 0.7 mm in size, of which one side is coated with indium-tin oxide (ITO) for interface finding. This is because a difference in refractive index of the IP-S resin and glass greater than 0.1 is needed for the 25x objective to detect the interface.

The medium size features 3D printing set solid is used. The parameters that can affect the print's integrity are the laser power (LP) and the scanning speed (SS) as well as the hatch/slice distance. The LP ranges from 0-100 % and the SS can range up to 625.000 mm/s, but will be tested first with 100.000 µm/s. A dose test will be performed to assess the optimal parameters visually, where a grid of pedestals was printed with varying LP in the horizontal direction and varying SS in the vertical direction. Hatching distance refers to the distance between each voxel in the lateral directions (x and y) while the slicing distance refers to the distance between each voxel in the vertical direction (z).

After establishing the ideal printing parameters, the next step is to perform the hydrogel growth experimentation. It will be performed and optimized on pedestals first and, if successful, will move onto more geometrically complex designs. During the literature review, we have opted for three distinct steps and designs:

- Pedestal
- Unit cell
- Scaffold, made of the aforementioned unit cells

4.2 Characterization

4.2.1 Contact Angle Measurement

The principle of the photoinitiator coating relies on the hydrophilicity of the surface of the 3D printed structure. Therefore, it is necessary to know if the 3D printed sample surface is hydrophobic or hydrophilic in nature. A contact angle measurement with water can be helpful to determine this and it was performed by an optical tensiometer.

A contact angle is the angle that a liquid forms at the interface of a liquid-solid-gas boundary. In this case the liquid is water and the angle it makes with the surface determines whether the surface is (super)hydrophobic, (super)hydrophilic, or neither. An angle of less than 90 degrees means the surface is hydrophilic, superhydrophilic if the contact angle is less than 10 degrees [55]. When the contact angle is higher than 90 degrees, the surface is hydrophobic, above 150 degrees it is classified as superhydrophobic [56].

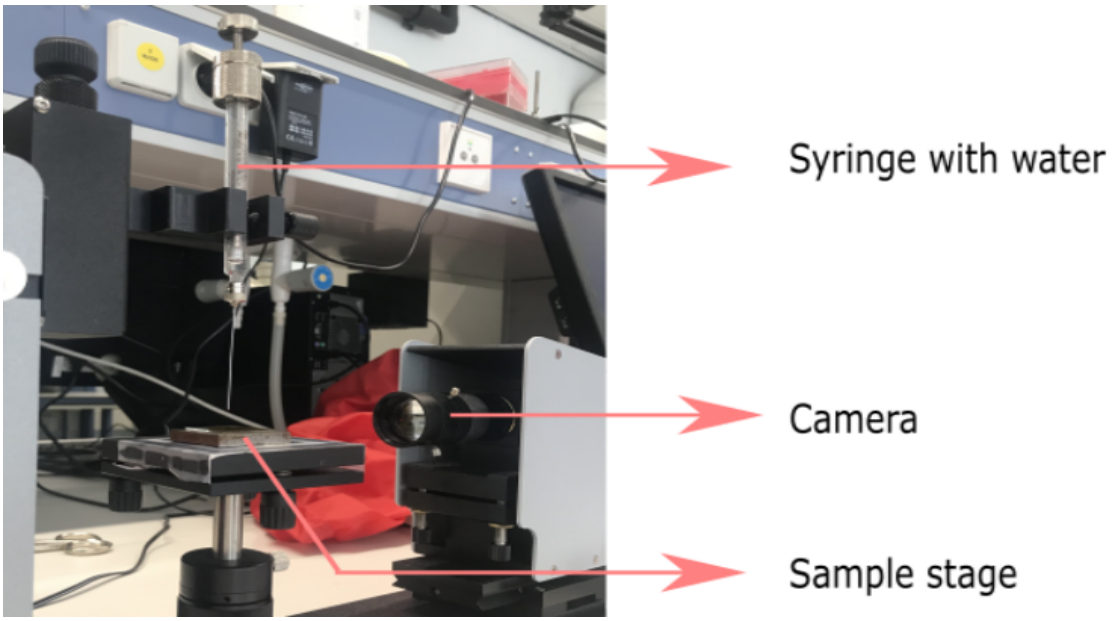

Figure 4.2: Optical Tensiometer

This static (sessile drop) contact angle measurement is performed with a camera. A water droplet of approximately 4 µL falls on the sample surface and the camera captures its shape. A numerical solution of the Young-Laplace equation is calculated with a software [57] in which the shape of the water droplet is fitted, a tangent line from the baseline of the drop to the edge is drawn and the contact angle is found. An example setup is shown in Figure 4.2.

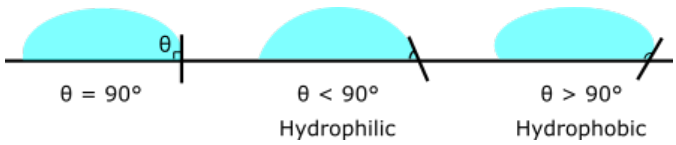

Figure 4.3: Water Contact Angle

4.2.2 Morphological Characterization

4.2.2.1 Scanning Electron Microscopy

The samples are primarily visualized in the scanning electron microscopy (SEM) for characterizing the surface topography. It is used to see if the newly 3D printed structures contain any defects, how the photoinitiator coating on the structures looks like, and how the hydrogel layer covers the samples.

A small electron beam is projected on the samples and a detector for secondary electrons is used to obtain information of the samples. These secondary electrons originate from inelastic interactions with atoms on the surface and have very low energies, only able to leave the sample from the top surface, thus bringing information of the surface with it. A software then creates images based on the intensity of the secondary electrons. A high vacuum chamber is needed to minimize the contamination of the electron beam with other molecules in air and attain a high resolution image. Due to the vacuum chamber, hydrogels are always air dried (minimum of 1 night) before characterization to prevent cracking of the hydrogel.

The non-conductive polymers (i.e. IP-S and PEGMA) are sputtered with gold particles to avoid charges on the surface when exposed to the electron beam as these charges can buildup and create white spots in an SEM image which will reduce the resolution. Typically, the sputtering process is done with 10 mA at 30 sec resulting in roughly a 10 nm thick layer of gold.

4.2.2.2 Atomic Force Microscopy

Another method to characterize the sample surface is an AFM measurement, where a micro-sized cantilever with a nano-sized tip scans the surface and records its topography. The Nanosurf Nanite B is used for this purpose. Imaging with AFM can be done via a "contact mode", where the tip touches the surface, and a "non-contact mode", where the tip oscillates close to resonance right above surface and is controlled via an amplitude feed-back loop. Imaging hydrogels with an AFM will be solely done in non-contact mode, because the cantilever tip would otherwise stick to the surface of the sample in presence of water. The tip used is of the type NCLR and in dynamic force mode. The topography of the hydrogel gives insight into the surface roughness of the hydrogel and the potential thickness of the hydrogel layer. After filtering, the roughness average (R_a) and the RMS (R_q) can be extracted from the images. Both parameters give an value of the average roughness in nanometres.

4.2.3 Mechanical Characterization

4.2.3.1 Compression Test

Compression test is performed to determine the stress/strain behaviour of a solid. Femtotools FT-NMT03 is used for this test. A flat micro-tip of 50 µm by 50 µm is used to plot a force-indentation curve from which the stiffness of the sample is derived. Before the actual measurement, the tip needs to be calibrated on glass without the sample.

The calculation of the E-modulus is done via Hooke's law, which is as follows:

$$E = \frac{\sigma}{\epsilon} = \frac{FL_0}{A\delta L} = \frac{Fh_0}{A_{tip\delta L}} = k\frac{h_0}{A_{tip}} \tag{4.1}$$

where k is the stiffness, h_0 the initial height of the sample and A_{tip} the area of the tip (L_{tip} x L_{tip}). Filling in the stiffness from experimentation will yield an E-modulus. A typical compression test graph is shown in Figure 4.5.a.

Compression testing will mainly be done on relative harder materials, as is with IP-S. IP-S is given to have an elastic modulus of E = 5.3 GPa as opposed to hydrogels (E ∼ 1-100 kPa), thus ideal for compression testing.

There are a few rules to follow when doing the compression test. This is to guarantee an indentation depth large enough without interference of previous measurements and the substrate underneath. The rules are:

1. The compression depth must be larger than 20x the surface roughness.
2. The compression depth must be maximum 10% of the sample height h.
3. The next compression location in planar directions must be 10x the indentation depth.

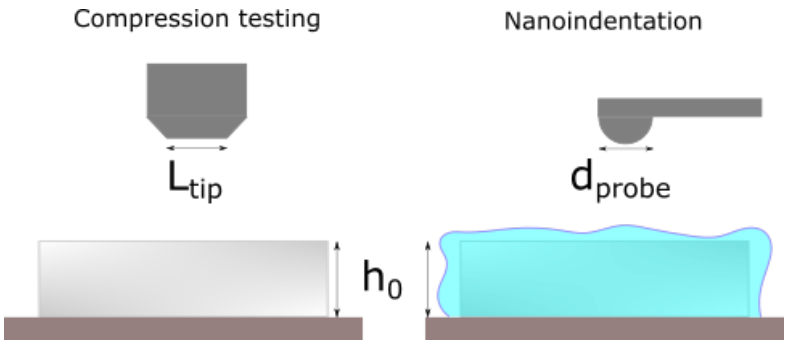

Figure 4.4: Compression testing and nanoindentation

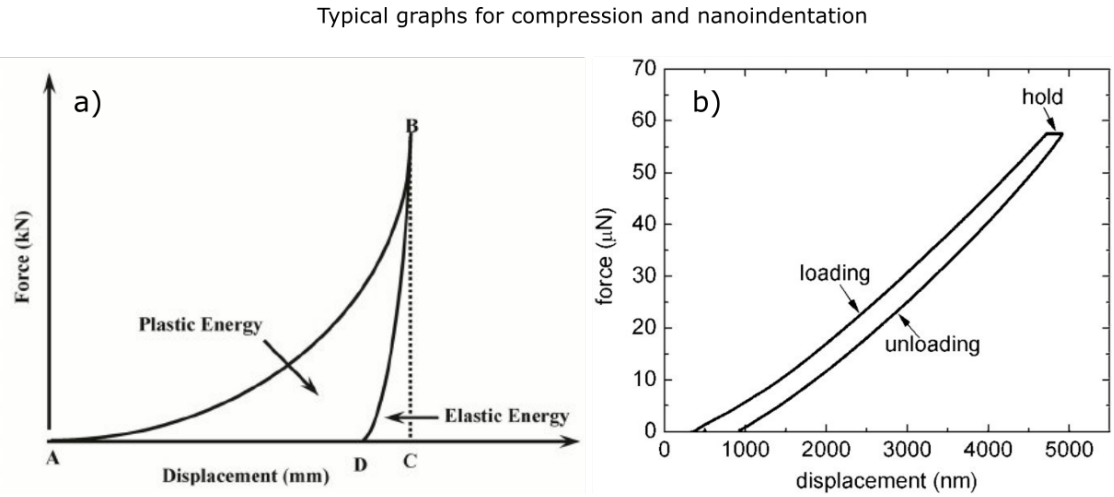

Figure 4.5: Typical graphs of a) compression testing [58] and b) nanoindentation [59]

4.2.3.2 Nanoindentation

Nanoindentation works in a similar fashion as the compression test. Instead of a flat tip, a round tip with a diameter of $d_{probe} = 50\,\mu m$ is used. This is because nanoindentation is performed on hydrogel, which is softer and has a much more irregular surface. The same force-indentation curve is made and the E-modulus is calculated by the software of the Piuma.

The spherical nanoindentation probe has a stiffness of $k = 0.023\,N/m$. This is one of the least stiff probe available and it can theoretically measure materials with elastic moduli down to 3 Pa. The maximum indentation height with this probe is $4\,\mu m$. A typical graph for nanoindentation is shown in Figure 4.5.b.

Calculation of the effective Young's modulus is done via a Hertzian contact model, where it assumes the materials in contact to be purely linear elastic and the Poisson ratio to be 0.5. This means that the loading phase of the measurement (Fig. 4.5.b) is used to derive the effective Young's modulus. The Hertzian contact model is chosen because it is far more suitable for soft samples like biological tissues and (bio)materials. In particular, the mechanical properties derived from the loading portion of the curve are representative of those of the virgin material, returning a constant modulus value regardless of the maximum load (or displacement) chosen for the measurements.

4.2.4 Chemical Characterization

4.2.4.1 Energy-Dispersive X-ray Spectroscopy

Energy-dispersive x-ray spectroscopy (EDS) is a characterization technique where the base elements of a sample surface can be imaged. EDS is performed in the same tool as where the SEM imaging is done. This is because the same electron beam in the SEM can also generate characteristic x-rays from the surface. These characteristic x-rays are formed because the electron beam can knock away an inner shell electron of an element, allowing an outer shell electron to fill the place and emit x-rays during the process. The energy of these x-rays depend on the atomic number of the element, thereby revealing the composition of the surface. EDS spectroscopies measure therefore the energy of x-rays in electron volt (KeV). Since the energies of the x-rays are characteristic of the difference in energy between the shells and of the atomic structure, each element has an unique number of electron volt associated with that element.

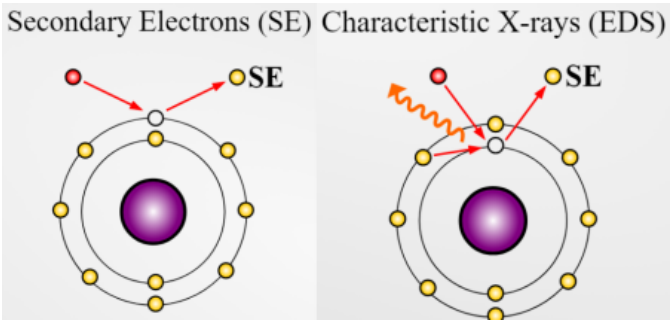

Figure 4.6: Secondary electrons and characteristic x-rays emitting from an atom [60]

4.2.4.2 Raman Spectroscopy

Raman spectroscopy is also a technique to characterize the composition of a sample surface, but different from elemental information in EDS. Raman spectroscopy relies on the inelastic scattering of photons when hitting a material. Here, an UV light laser illuminates a sample surface and scatters once hitting the surface. The laser, unlike EDS, does not excite the molecules in the sample, but instead creates a dipole moment in the molecule and exchange energy. The back scattered photons that leave the sample will have their energy shifted from which information of bonds present in the sample are extracted. The scattered UV light, shifted in terms of energy and frequency, is not a good parameter for comparison with other measurements as it will always depend on the initial wavelength of the laser which is arbitrary. Instead, in Raman spectroscopy the parameter is always the Raman shift which refers to how much the original wavelength has shifted in its energy and frequency. The Raman shift can easily be calculated with:

$$\Delta v(cm^{-1}) = (\frac{1}{\lambda_0(nm)} - \frac{1}{\lambda_1(nm)})\frac{(10^7 nm}{(cm)} \tag{4.2}$$

with Δv the raman shift, λ_0 the initial laser wavelength, and λ_1 the scattered wavelength. An increase of energy in the scattered photons is called Stokes scattering while the reverse is called anti-Stokes scattering (Fig 4.7). The result of a raman spectroscopy is therefore a spectrum with different wavenumbers (inverse of wavelength), with each bond covering a part of the spectrum.

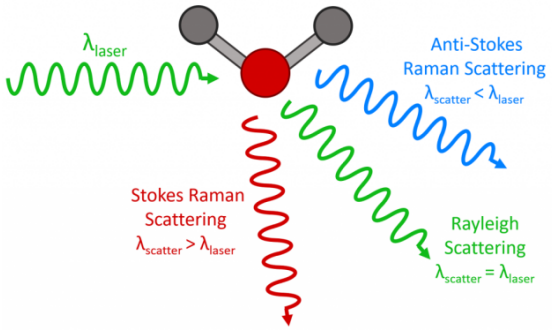

Figure 4.7: Scattering of photons in Raman spectroscopy [61]

The Raman spectroscopies are performed with an UV light of 514.51 nm and an 50x objective, using an integration time of 10 second, scanned with different laser powers, ranging from 0.1% to 50%.

Chapter 5
Results and Discussion

The results of each phase of the thesis are presented here and interpreted. The polymer micro-structure fabrication will be discussed. Further sections include the characterization of the photoinitiator coating and the grown hydrogel layer.

5.1 Polymer micro-structure fabrication

The parameters that mainly affect the structure integrity are the laser power (LP) and scanning speed (SS). A first assessment of the parameters was a dose test, where a grid of pedestals with bars is printed (Fig. 5.2). The hatching/slicing distance were kept the same in the standard printing configuration of the Nanoscribe. Hatching distance is 0.5 µm and slicing distance is 1 µm. The dimensions of the pedestal used in this thesis are 100x100x50 µm (l/w/h).

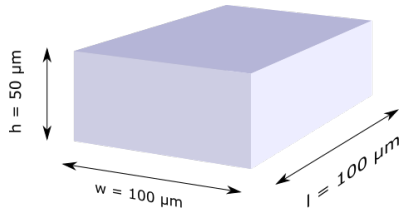

Figure 5.1: Pedestal dimensions

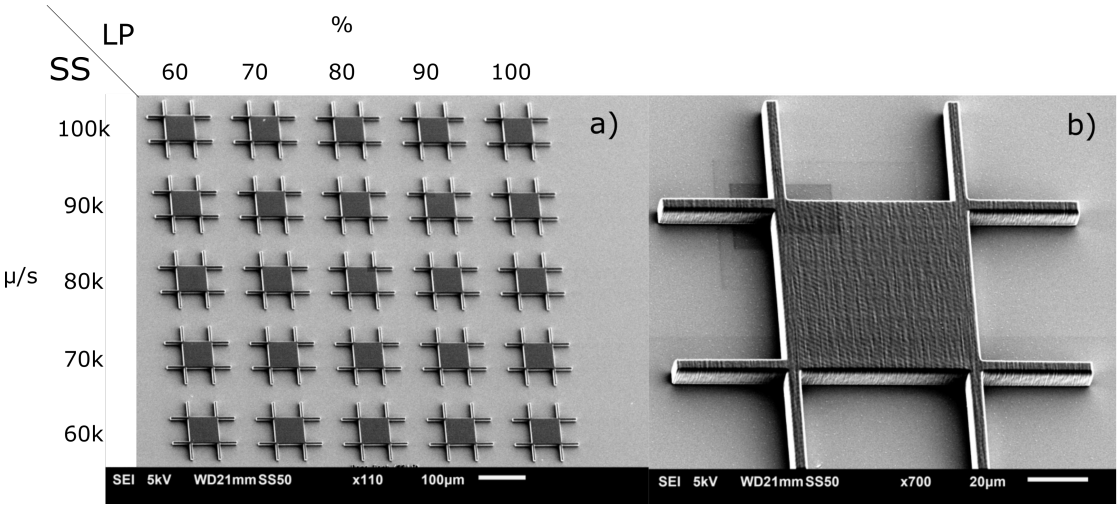

Figure 5.2: a) SEM image of a dose test on pedestal structures. The laser power is shown on the horizontal axis, ranging from 60 to 100%. The scanning speed is shown on the vertical axis, ranging from 60k up to 100k µm/s. b) A single pedestal with no printing defects

The laser power ranged from 60 to 100% while the scanning speed ranged from 60k to

100k µm/s. Visually, there are no defects to be found on any of the pedestals. Defects that could happen are inadequate polymerization and bubble formation, but are not present. There has been opted for the printing parameters 80LP/80kSS because no printing defects were observed in the pedestals around these parameters.

The properties of the pedestals were then evaluated. Since the experimentation relies heavily on the wettability of the sample and no information was given, a water contact angle measurement was performed. First, the IP-S photoresin was spin-coated on a glass substrate and subsequently polymerized under an UV light spot, a an light intensity of 1000 mW/cm^2 and a wavelength of 360 nm, at 80% power and at a distance of 1 cm. Then the contact angle measurement was performed. In the measurement, the contact angle of two sides can be seen. An average is taken from the left contact angle and the right contact angle. The resulting contact angle was 77.71°± 0.06°(n = 69), which means the IP-S polymer surface is hydrophilic.

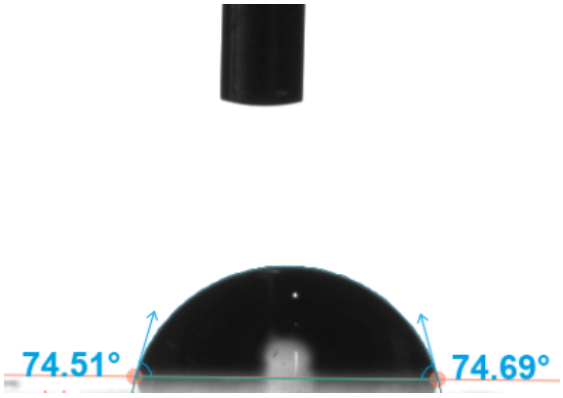

Figure 5.3: Contact angle measurements from both sides of the drop.

The other property is the elastic modulus of IP-S. As previously mentioned, the E-modulus is given by Nanoscribe to be E = 5.3 GPa, but printing parameters can influence and impact the material properties. Since our printing parameters were chosen at 80LP/80kSS, the E-modulus could be different. Compression testing was performed to evaluate the potential new E-modulus. The minimum compression depth is 5 µm and each compression was placed 50 µm apart from each other. The compressed sample is a pedestal of 100x100x50 µm (l/w/h) and the compression is performed over multiple pedestals, with a maximum of four compressions on each pedestal.

Femtotools measured an average stiffness of k = 143 kN/m ± 28.8 kN/m (n = 36) which resulted in an average E-modulus of $E_{average}$ = 2.85 GPa ± 0.575 GPa of the IP-S, when using Eq. 4.1 in Chapter 4.2.3.1. The obtained force-displacement curve (Fig. 5.4) shows plastic deformation and little elastic deformation, as described in Figure 4.5.

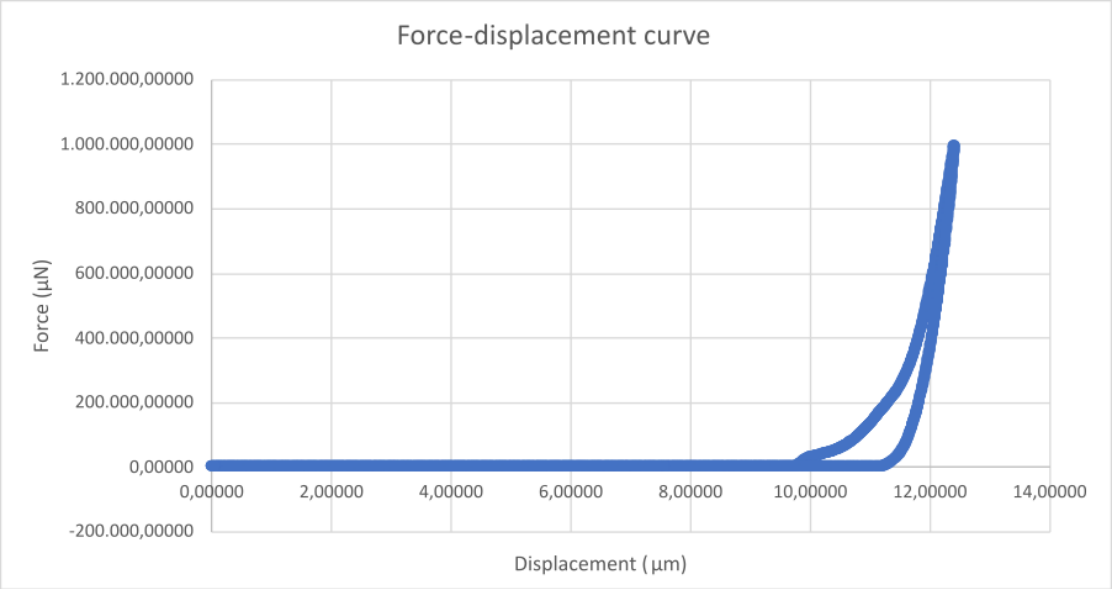

Figure 5.4: Representative force-displacement curve from compression testing on IP-S

The next step was the production of the unit cells and the scaffolds. The unit cell design was 80x80x80 µm with cylindrical beams of 15 µm in diameter. The scaffold is an arrangement of the unit cells, placed in a 3x3x2 configuration (Fig. 5.5). No defects or issues were encountered when printing with the same parameters.

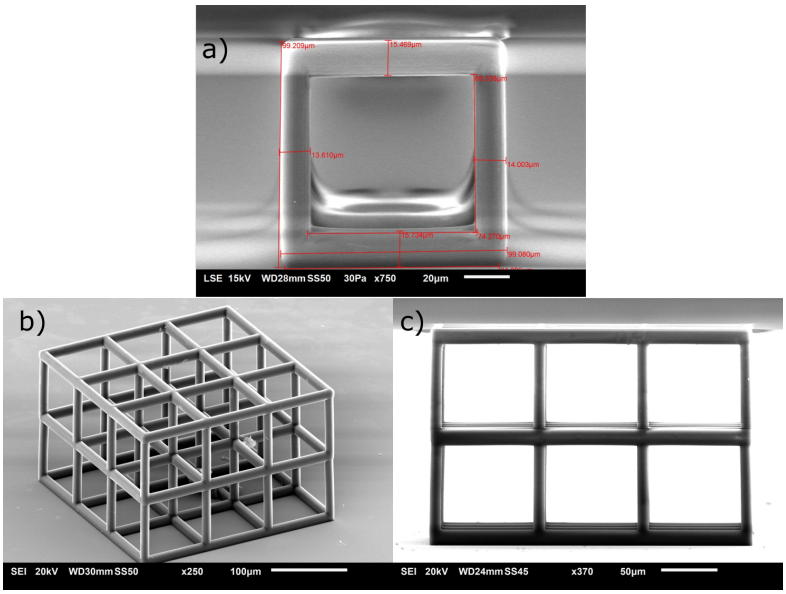

Figure 5.5: a) Unit cell b) Scaffold c) Scaffold, side view

5.2 Photo-initiator Coating

A photo-initiator bath was used to apply the photo-initiators onto the structures. The initiators are mixed with an organic solvent first with a 10 % w/v distribution. The baths will consist of Irgacure184 dissolved in IPA.

Parameters in this step are the concentration of photoinitiators, the initiators and solvents itself, and the photo-initiator bath time.

This part of the experiment follows the same methodology of Yu et al. [49], where the samples are put in this photo-initiator bath for 3-5 minutes. After the bath, the hydrogel growth step is performed.

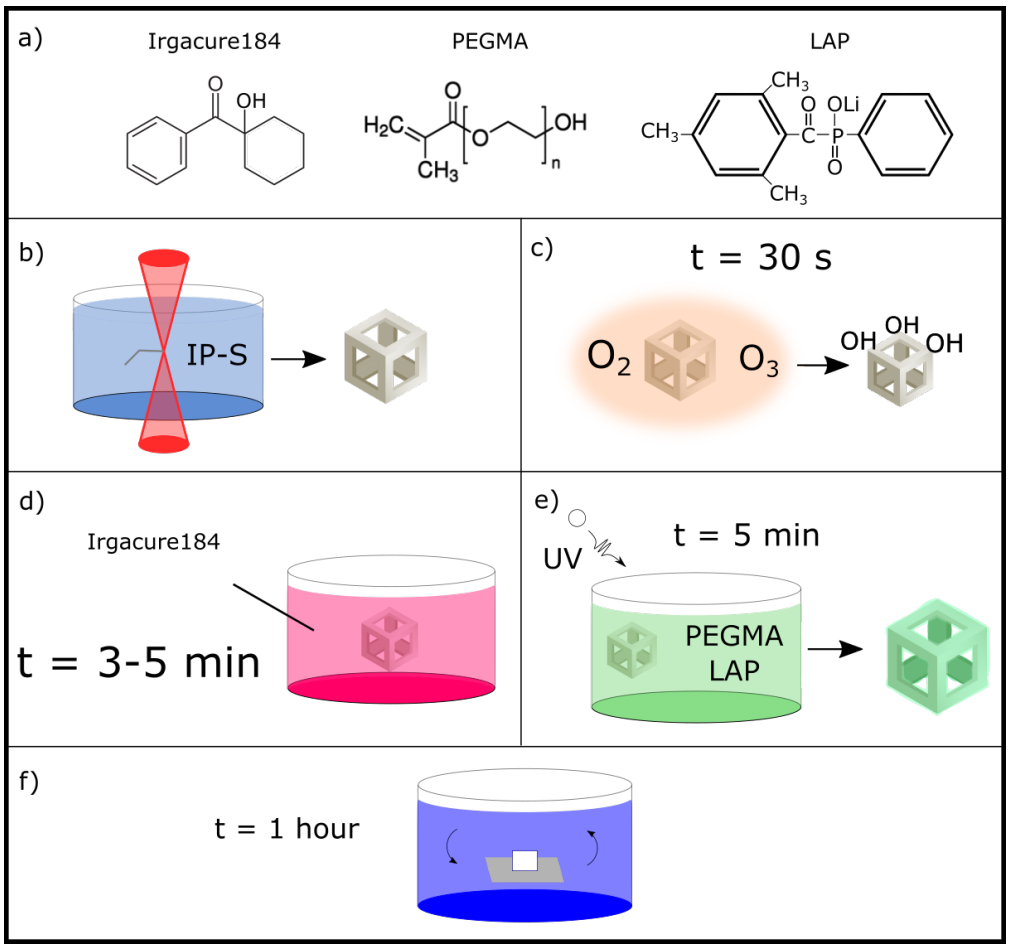

Figure 5.6: Protocol 1: an adaption on the works of Yu et al. [49]. a) Chemical structures of I184, PEGMA, and LAP. b) 3D printing IP-S structures via 2PP. c) Surface activation via oxygen plasma. d) Hydrophobic photoinitiator bath (I184) of 3-5 minutes of the IP-S structures. e) Hydrogel growth under UV light immediately after photoinitiator bath in a PEGMA + LAP precursor solution for 5 minutes. f) Water plunge to remove unpolymerized hydrogel solution

In this phase the photo-initiator coating is applied on the printed structures. The structures sample surface is first activated with oxygen plasma for 30 seconds (Fig. 5.6.c). Then the samples are plunged into a photo-initiator bath of hydrophobic initiators in an organic solvent (Fig. 5.6.d). The photo-initiator bath consists of 10% w/v I184 in IPA. The time was varied between 3 and 5 minutes, after which the hydrogel growth started (Fig. 5.6.5). The hydrogel precursor solution consists of 1% w/v LAP in 20% w/v PEGMA in water. The experiments involved only pedestals because of the simplicity of the shape. If successful, testing the same protocol with unit cells and scaffolds follows. Here, the initial parameters that could be changed were the concentrations of the photo-initiators in the solvents and the bath time.

During this phase, when the samples were taken out of the initiators bath, the initiators disappeared from the sample whenever it advanced to the next step too soon, meaning 3-5 minutes was not enough time for the initiators to settle and to be absorbed by the IP-S. Furthermore, the I184 initiators were covering the entire substrate and the samples, leading to over-polymerization and no specificity of the hydrogel crosslinking on the samples in the next step.

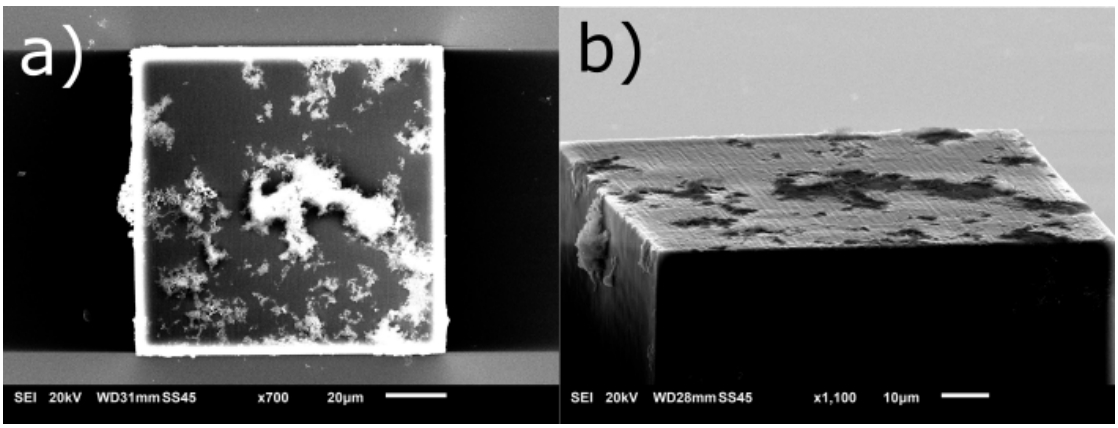

Figure 5.7: a) SEM image of Irgacure184 that was left on an IP-S pedestal after one overnight bath, rinsed, and air dried overnight again. Top view. b) Oblique view

The first issue was resolved by increasing the bath time to 12+ hours (overnight) and adding air drying as an extra step. Small amounts of solvent that were still left on the substrate would evaporate and the initiators could settle on the samples (Fig. 5.7). The second issue of non-specificity could be resolved by adding a rinsing step, where the samples after the bath were rinsed with IPA before being air dried (Fig. 5.8). These steps were added right after the photoinitiator bath step in Figure 5.6.d.

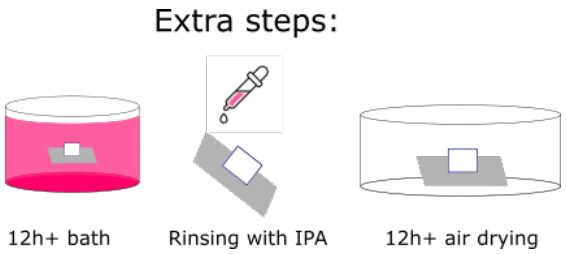

Figure 5.8: Extra steps that were implemented into the process.

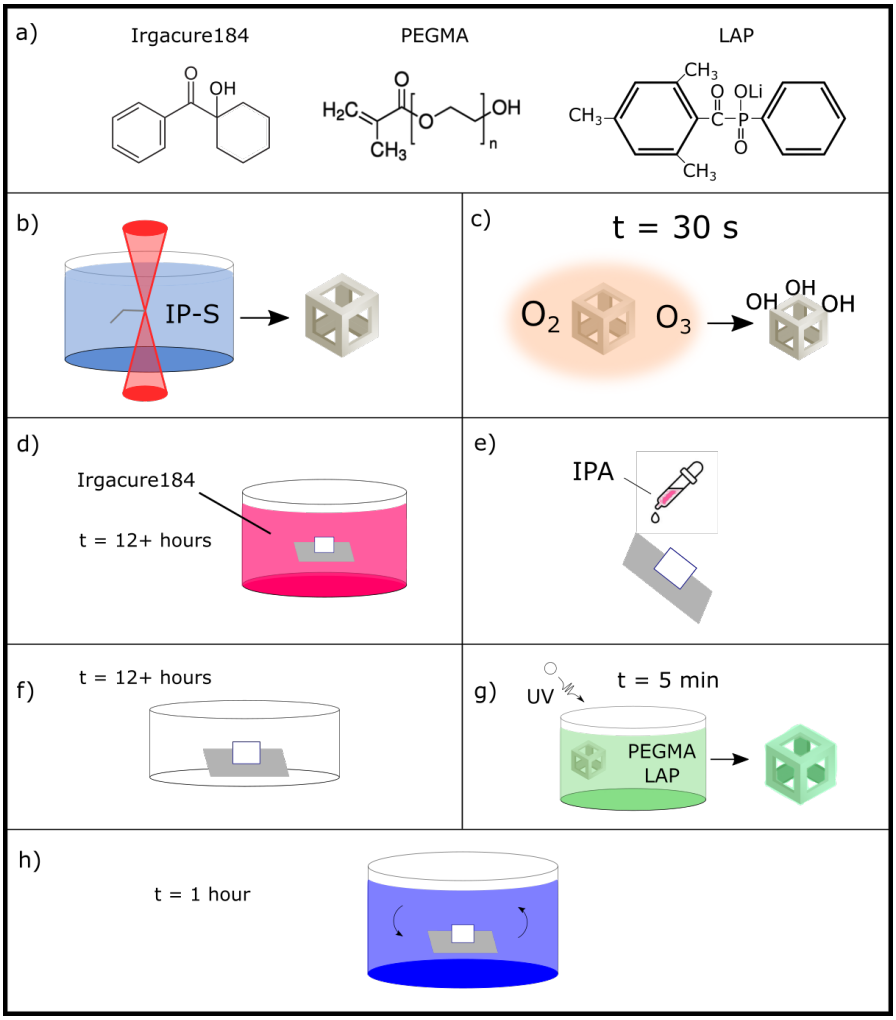

Figure 5.9: Protocol 2. a) Chemical structures of I184, PEGMA, and LAP. b) 3D printing IP-S structures via 2PP. c) Surface activation via oxygen plasma. d) Hydrophobic photoinitiator bath (I184) of 12+ hours (overnight) of the IP-S structures. e) Rinsing the sample with IPA when taken out of the photoinitiator bath f) Airdrying the samples for 12+ hours (overnight) g) Hydrogel growth under UV light immediately after photoinitiator bath in a PEGMA + LAP precursor solution for 5 minutes. h) Water plunge to remove unpolymerized hydrogel solution

Extra characterization was performed to confirm the presence of I184 on IP-S pedestal structures. With EDS and raman spectroscopies, the presence of I184 on the sample surface can be verified.

EDS is performed on pedestals with, visually confirmed, I184 coverage. A comparison between before and after the photo-initiator bath is performed by EDS (Fig. 9.2) in Appendix B.

Unfortunately, a comparison of EDS spectra before and after the bath does not contribute to the verification of I184 on pedestals. The distribution of all the elements detected does not help either (Appendix C). Aside from the predictable elements such as carbon and oxygen, and the three elements of ITO glass, there is only element which stood out. Sodium appears to be abundant in both cases and could belong to the soda lime glass of the sample or be a component of the IP-S polymer. Two other peaks were also present, but in lower amount. Highlighted in the figure as peak A and peak B, the x-ray energies are 1.25 keV and 1.5 keV respectively. From the periodic table, these peaks overlap with some elements. Peak A with 1.25 keV can be attributed to the first shell of magnesium (κ_a = 1.253 keV) or second shell of arsenic (λ_a = 1.282 keV), while peak B with 1.5 keV can be assigned to the first shell of aluminium (κ_a = 1.486 keV) or second shell of bromine (λ_a = 1.480). The two peaks are most likely also part of the soda lime glass, like sodium, and not an indicator for I184.

Given the amount of x-ray detection of indium and tin, sodium is more likely to be an element in the IP-S and given the molecular structure of I184, sodium is impossible to be an indicator for I184. With no significant difference in the distribution or peak heights, EDS did not support the claim that I184 was present on the IP-S.

Another characterization has been performed to confirm the presence of I184 on IP-S, which is a Raman spectroscopy. Raman spectra were acquired from different samples: IP-S polymer, I184 initiator, IP-S with I184 on top, and another IP-S with I184. Background filtering was performed by subtracting the IP-S signal spectra from the combined signal spectra of IP-S and I184 in the frequency domain and transforming it back to the time-domain. A list of Raman correlations to different bonds can be found in Appendix D. From the spectra in Fig. 5.11.a and 5.11.b, the only peak that appears in the IPS+I184 but not in the IPS alone is the one at 700 cm^{-1}, which also overlaps with an I184 peak. This peak at 700 cm^{-1} can belong to a strong sulfur bond (670-780 cm^{-1}) or a moderate carbon-carbon aliphatic chain (630-1250 cm^{-1}). I184 does not contain any sulfur atoms nor is it aliphatic (pure hydrocarbon chain). However, the I184 Raman spectrum shows three distinct peaks, increasing in intensity between 600 and 800 cm^{-1}. These three peaks have a similar shape as the 700 cm^{-1} peak found earlier. Since these peaks are not associated with any bonds in I184 but does appear in the Raman spectra, no definite conclusion can be made.

An argument could be made for the 600-1000 cm^{-1} peaks regarding the intensity of the signal. If we compare the peaks *relatively* to each other, it appears that the peaks between 200-400 cm^{-1} and 1400-1600 cm^{-1} have decreased in intensity, or in other words,

the peaks between 600-1000 cm^{-1} have increased relatively to other peaks that are not associated with I184. In addition, the 1000 cm^{-1} peak in I184 corresponds to aromatic rings of which I184 has two of and is also the strongest signal from I184.

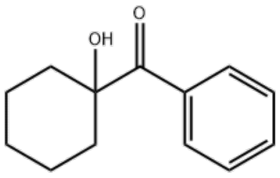

Figure 5.10: Molecular structure I184

Based on this observation we conclude that the photoinitiator I184 is present as a coating when taken out of the photoinitiator bath.

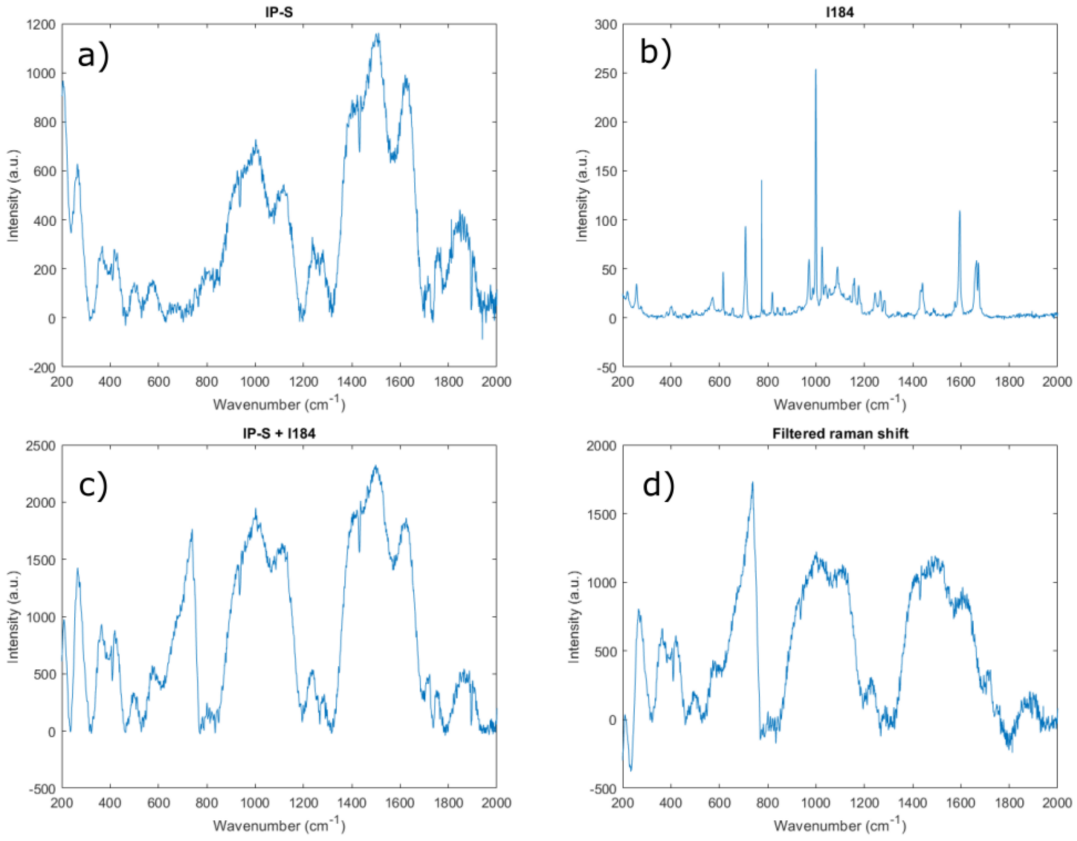

Figure 5.11: a) IP-S Raman spectrum b) I184 Raman spectrum c) IP-S + I184 Raman spectrum, where the samples were directly taken out of the photoinitiator bath d) Filtered IP-S + I184 Raman spectrum

Although the Raman spectra presented in this section are clear, a major problem in the raman spectroscopy on photo-initiators is that the employed UV laser also activates the

photo-initiator on the sample. Consecutive measurements at the same location would therefore yield less strong signals.

5.3 Hydrogel Growth

The last step of the experiment consists of crosslinking a hydrogel layer on the samples, taken from the photo-initiator baths. The UV light source used for this is an UV oven (UV light curing unit, DentalFarm). The hydrogel pre-cursor solution is 20 % w/v PEGMA in DI water mixed with 0.1 % w/v LAP photo-initiator. The samples are submerged in a water bath to diffuse the excess pre-cursor solution away from the samples.

Tunable parameters in this phase are the concentration of the photoinitiator, concentration of the hydrogel monomer, curing time, UV light intensity, and the time in the plunge bath after curing.

5.3.1 Pedestals

The last phase of the developed protocol is crosslinking the hydrogel on the samples. At the start of this phase, an UV oven (Dentalfarm) was proposed as the light source for crosslinking. However, after many failed attempts to grow the hydrogel we concluded that the UV oven was inadequate for crosslinking hydrogels due to a defect of the UV lamps. Another UV source was used, an UV spot. This one was better suited because the height and the power of the light could be adjusted and therefore the intensity.

The setup of this part consists of a UV spot light, set at a 3 cm distance above the sample height and illuminated for 5 minutes. The maximum intensity of the light is 10.000 µW/cm^2, but since the intensity of light decreases quadratically with the distance, the intensity of the light hitting the sample is only at 1000 µW/cm^2.

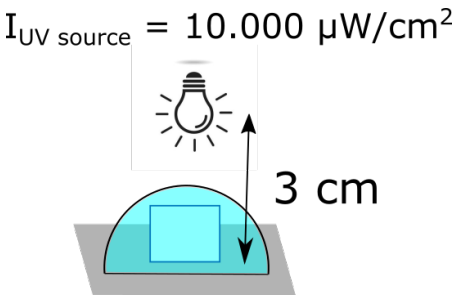

Figure 5.12: Schematic of the setup for hydrogel crosslinking under UV light

During the project, a few issues were encountered. First, bubbles were forming on top of the pedestals (Fig. 5.13). These bubbles were spread unevenly across the surface, but was eventually resolved by mixing the photo-initiator bath solution for at least 2 hours with a magnetic stirrer when preparing the hydrogel precursor. This is most likely because the LAP photo initiators were not stirred sufficiently, therefore agglomerating and sticking to the samples. After curing, the agglomerated photoinitiators appear as bubbles on top of the substrates.

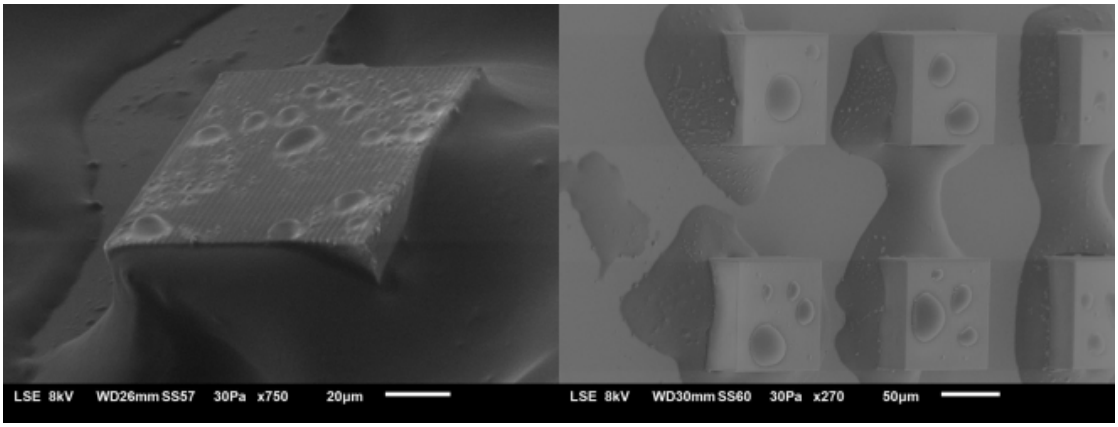

Figure 5.13: Bubble forming on the samples

Secondly, hydrogel was either crosslinked across the whole substrate, or absent. Specific crosslinking on samples is difficult because there are many parameters in this step that can influence the crosslinking process, such as the concentrations of hydrogel monomers and photoinitiators, the UV curing time, and the UV light source intensity.

In order to understand the role of each photo-initiator during the process, some control tests were performed. Hydrogel crosslinking was performed where the hydrophobic initiator I184 in the updated protocol in Figure 5.9.d was omitted or the hydrophilic initiator LAP in Figure 5.9.g was omitted (see below).

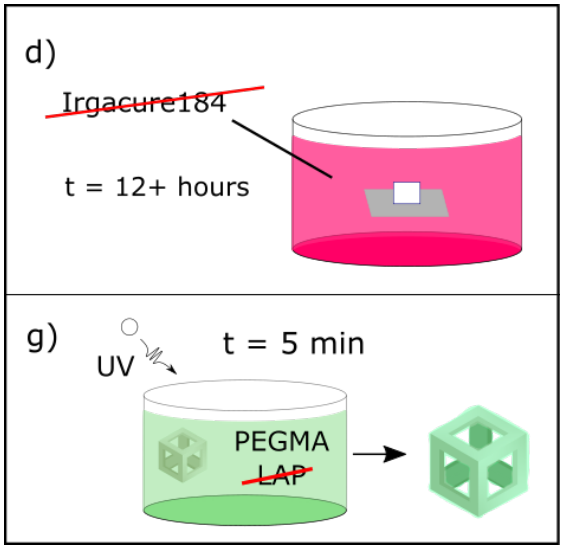

Figure 5.14: d) Irgacure184 is taken out of the bath in order to understand its effect g) LAP is taken out of the hydrogel precursor in order to understand its effect

Taking out the I184 means that no FRP reaction can start at the surface sample, the surface-initiated method, which is the focus point of this project. From SEM images, we can clearly see that taking out the I184 would not result in any hydrogel layers on the samples (Fig. 5.15.a), whereas taking out the LAP still resulted into hydrogel crosslinking. In fact, in Fig. 5.15.c and d we can clearly see an improvement of hydrogel crosslinking across all the samples.

LAP was used because it would also initiate the polymerization of the hydrogel at the sample surface and in the precursor. However, from this control test it was clear that leaving out the LAP had beneficial results for hydrogel layers, as can be seen in Figure 5.15. Figure 5.15 shows a comparison between a pedestal where I184 was omitted and one where LAP was omitted. A clear, distinguishable layer of hydrogel can be observed on the one without LAP. Not only does the hydrogel cover the pedestals in this configuration, it is also restricted to a certain area around the pedestal, which means an increase specificity of the hydrogel growth.

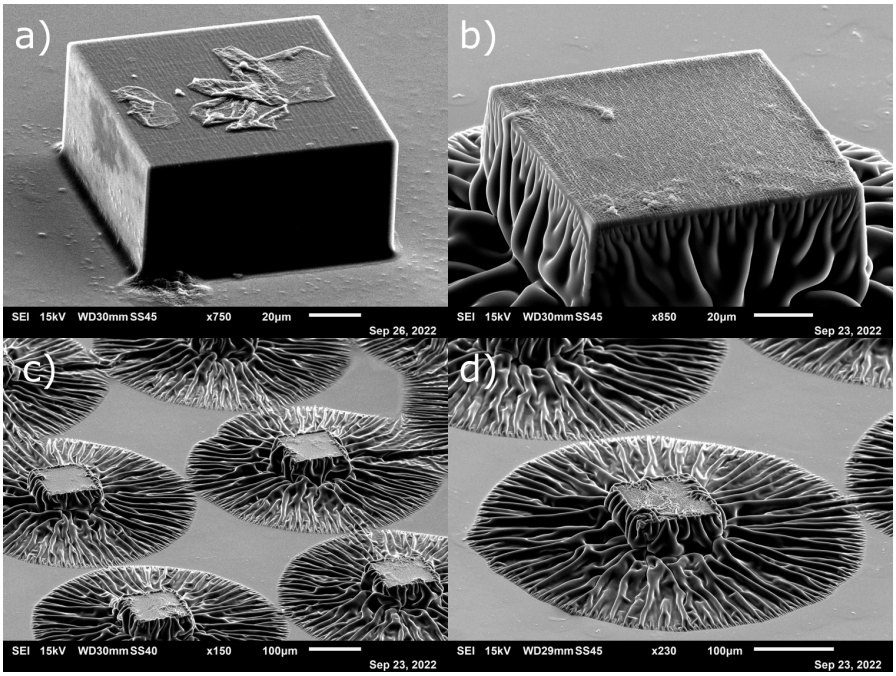

Figure 5.15: a) SEM image of a pedestal where the I184 was taken out b) LAP was taken out c) and d) Not adding LAP increased the hydrogel crosslinking on pedestals throughout the samples

From here onward, the method had been modified by not including LAP anymore in the process. The hydrogel precursor concentration is thus set at 20% w/v PEGMA in water only (see below).

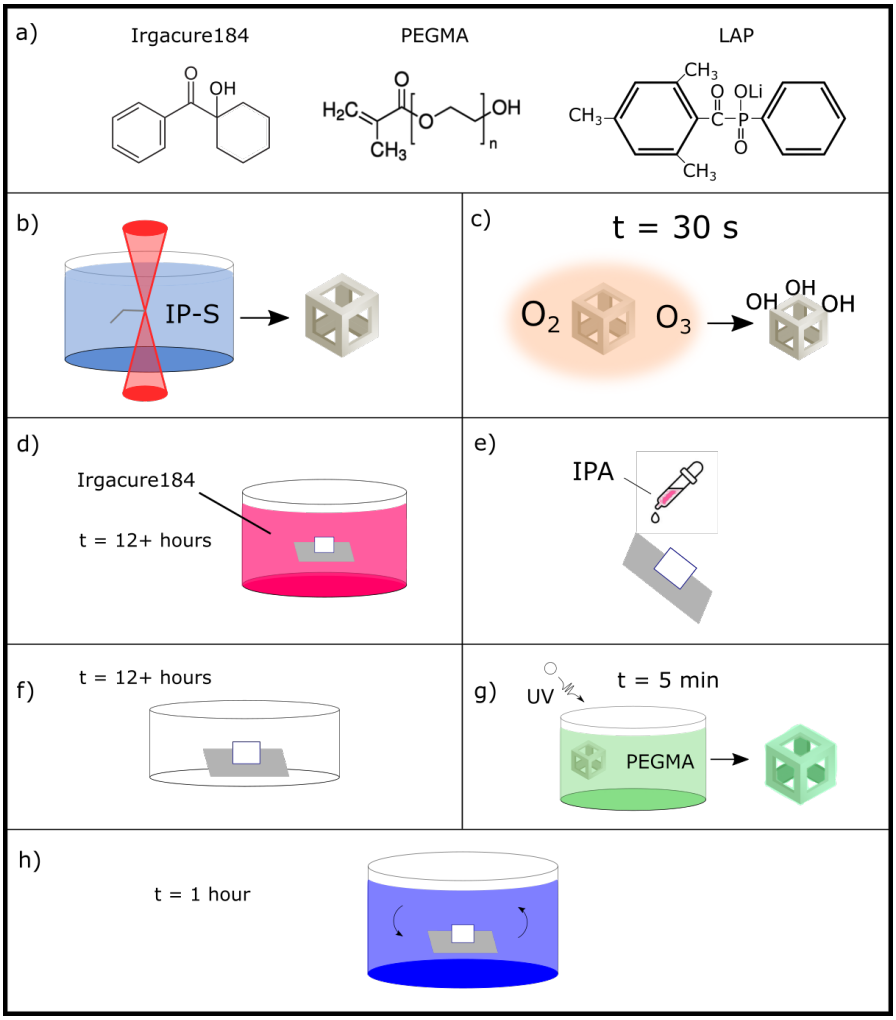

Figure 5.16: Protocol 3. a) Chemical structures of I184, PEGMA, and LAP. b) 3D printing IP-S structures via 2PP. c) Surface activation via oxygen plasma. d) Hydrophobic photoinitiator bath (I184) of 12+ hours (overnight) of the IP-S structures. e) Rinsing the sample with IPA when taken out of the photoinitiator bath f) Airdrying the samples for 12+ hours (overnight) g) Hydrogel growth under UV light immediately after photoinitiator bath in a PEGMA precursor solution for 5 minutes h) Water plunge to remove unpolymerized hydrogel solution

Hydrogel skins have been created on pedestals and it is important to know which is their average surface roughness. AFM is performed on hydrogels polymerized on pedestals. A common issue with AFM surface scans, even in tapping/dynamic mode, is that the tip often snaps onto the wet hydrogel, sticking to it due to strong polar bonds. This often happens halfway through scans and therefore only provides half of the imaging data. After generating an AFM image, the image is filtered to separate the surface topography from background signal. After filtering the surface roughness values R_a and R_q are extracted. R_a is the average of the height deviations from the mean line while R_q is the RMS average of the height deviations from the mean line. Gwyddion is the software used to do the AFM data processing. A 2D FFT filtering is done where the

background noise signal is filtered out.

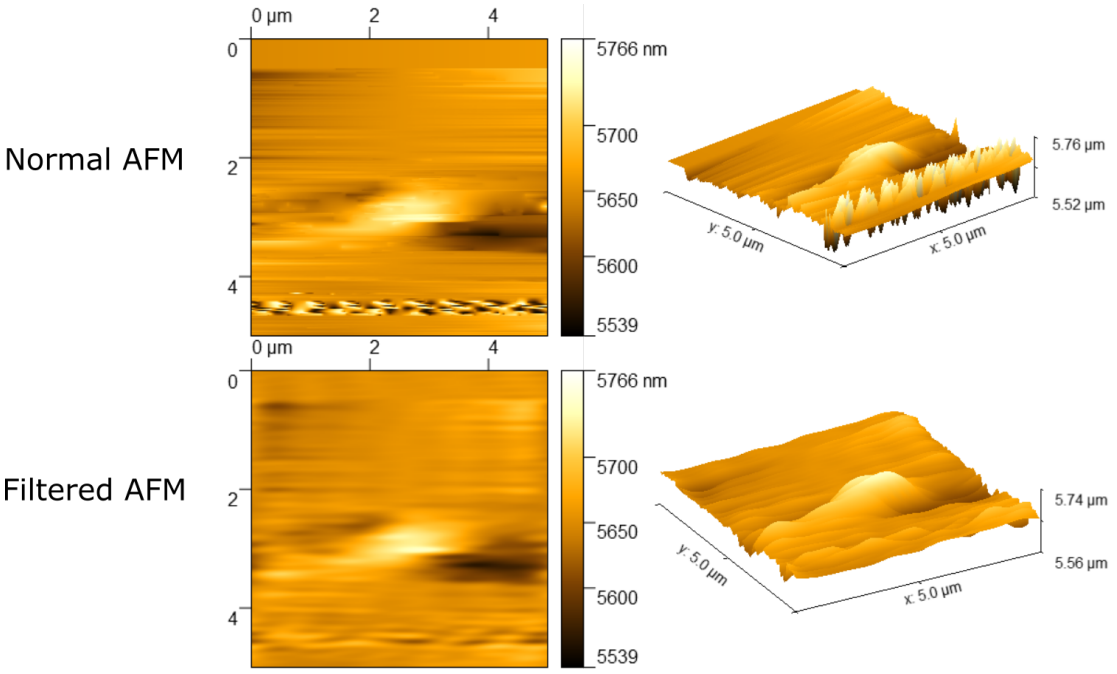

Figure 5.17: AFM images of PEGMA hydrogel grown on IP-S pedestal

The extracted surface roughness values for R_a and R_q are over multiple samples are (n = 6):

Normal AFM: $R_a = 15.17\,\text{nm}$, $R_q = 22.67\,\text{nm}$,

FilteredAFM: $R_a = 13.09\,\text{nm}$, $R_q = 19.46\,\text{nm}$,

The Young's modulus of the same hydrogel skins was also characterized by using nanoindentation in aqueous environment, because the probe cantilever can break due to large adhesion forces in dry conditions and because these hydrogels are intended to bu used in cell media.

During the analysis, a Hertzian contact fitting is used for a spherical contact point with a surface, only taking into account the elastic property of the hydrogel and Van der Waals forces during the loading phase is neglected. A standard Poisson ratio of $\nu = 0.5$ is used. When applying the Hertzian model fit, the curve to be fitted is 90% of the maximum load (P_{max}) of the loading part down to 15% of the P_{max}.

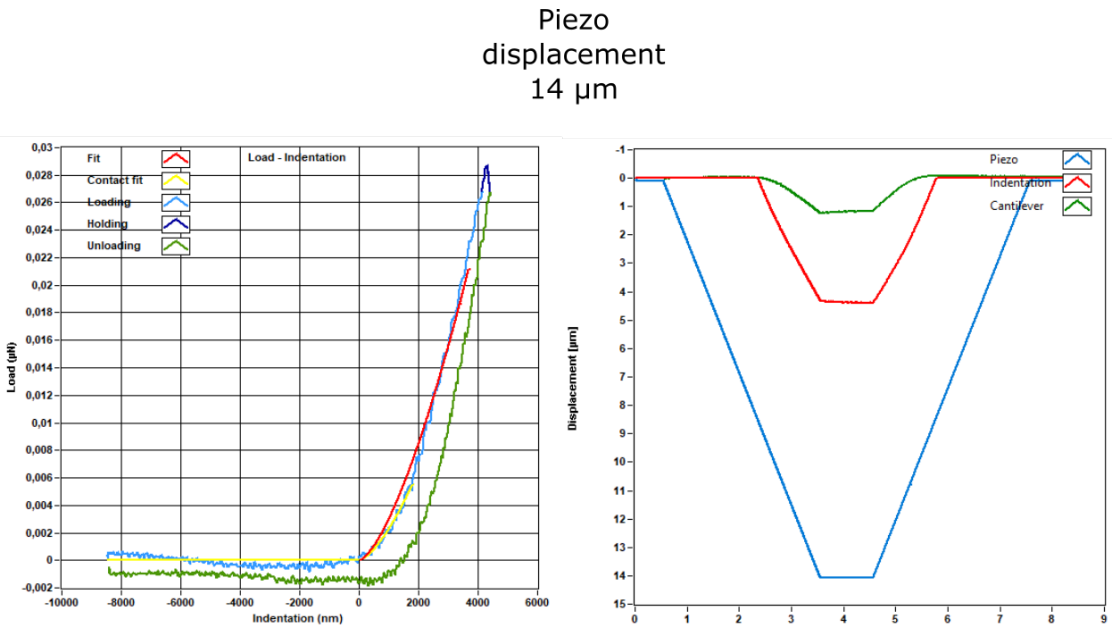

Figure 5.18: Representative load/indentation plot with Hertzian fit and related cantilever/piezo displacements as well as indentation depths.

Using a piezo displacement of 14 µm, we obtained an indentation depth of 4 µm. The average E-modulus of a 20% w/v PEGMA in water was found to be 429.3 Pa ± 93.7 Pa (n=16), which is very close to the Young's modulus of the brain tissue.

Characterization with white light interferometer has also been conducted, but the results lacked big data gaps containing zero information. Appendix E can be visited for further information.

5.3.2 Unit cell and scaffold

The same protocol is applied to the unit cell. The unit cells are trickier to grow hydrogels on because the surface area is considerable less than the pedestals due to the presence of large pores. The first

First the monomer concentration was explored and while it is obvious that more monomers means more crosslinking, it was not known if lower concentrations could lead to similar results. To shed some light on this matter, monomer concentration tests have been conducted. Since the standard approach of 20% w/v PEGMA at 5 min shows sufficient hydrogel crosslinking, the monomer concentrations have thus been lowered. Tests with monomer concentrations of 1,5,10,and 20% PEGMA were carried out. Below, the different outcomes were captured in SEM images.

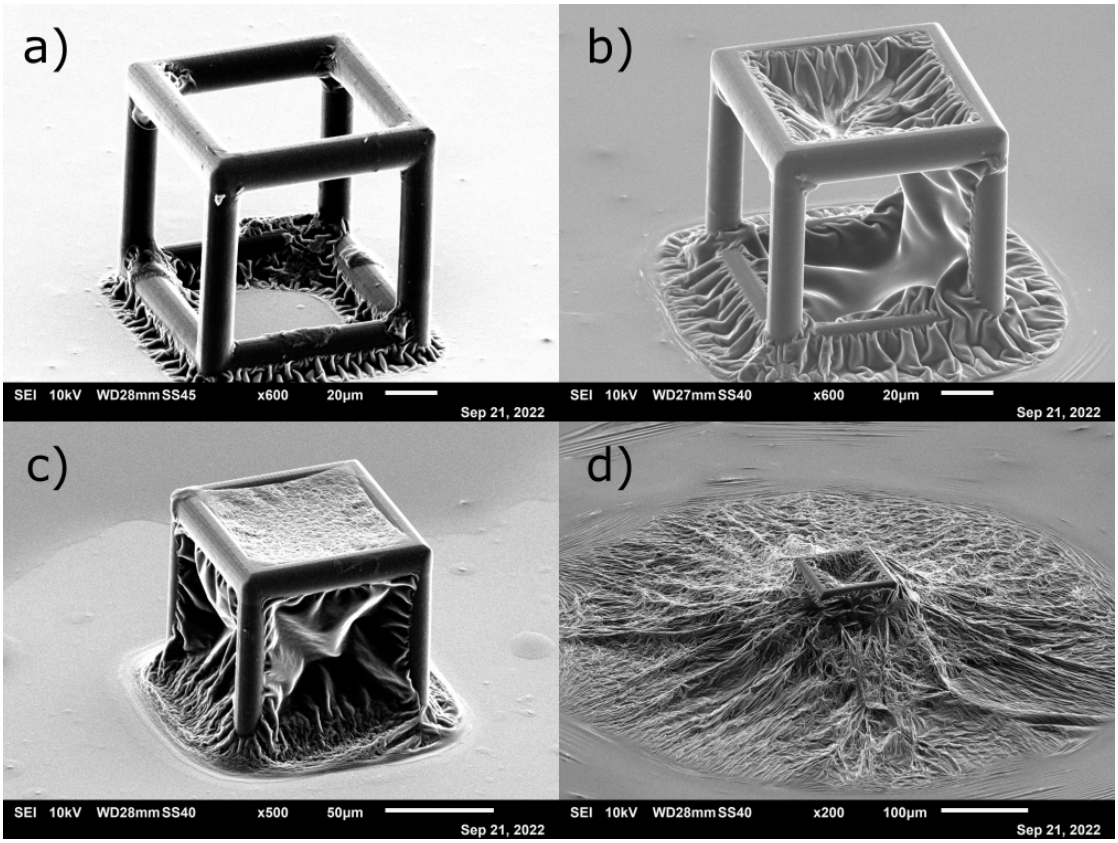

Figure 5.19: PEGMA monomer concentration test. a) 1% b) 5% c) 10% d) 20%. Other parameters were held constant.

Distinction between the different degrees of polymerization can be seen, where 20% seems to induce over-polymerization of the hydrogel. At 10% there is less crosslinking and it is more centered on the unit cell itself, while in the 5% and 1% PEGMA solutions the hydrogel crosslinking is limited to the base of the unit cell or covering the unit cell partially. Lowering the monomer concentrations means that in FRP a polymer chain during propagation is surrounded by less monomers. Propagation is therefore less likely to continue with each propagation step. Termination of FRP is also more likely to happen which results in hydrogel skins which do not grow beyond the base of the unit cell.

Optimizing for the power of the laser would be redundant, as the intensity of different levels of power of the UV light are close to each other (Fig. 5.20). The plot is calculated with the inverse-square law for intensity:

$$Intensity = \frac{Power}{4\pi r^2} \tag{5.1}$$

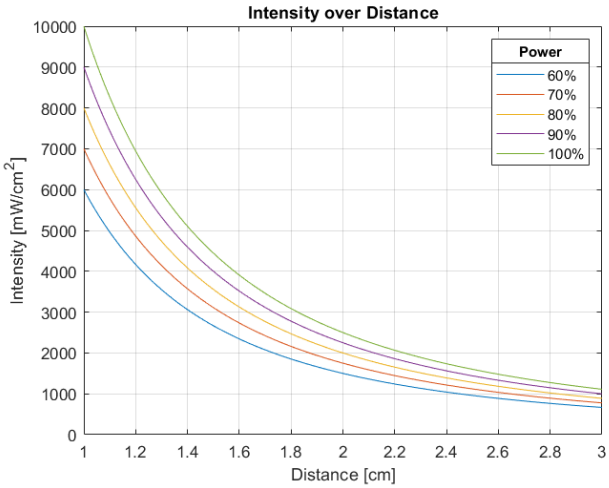

Figure 5.20: Intensity of the UV light source plotted over the distance

During the crosslinking, a problem that arose was the forming of hydrogel films, clogging the pores. It was not possible to resolve this issue by changing the different parameters mentioned in this paper. Clogging occurred at the lowest dose setting, while at higher dose settings the hydrogel fully clogged the structures.

Another parameter optimized is the time under the UV light. 5 minutes irradiation was considered too long, because much of the hydrogel crosslinking continues beyond the IP-S structure as seen in 5.15.c/d and 5.19.d. Therefore, the time has been scaled down between 90 s and 210 s, while other parameters were held constant. In Figure **??**, the resulting SEM images can be seen.

A high variance of consistency can be observed. Lower amount of curing times did not consistently result in less crosslinking. Instead, the amount varies between each curing time. For example, at 90s the scaffold appears to lack any hydrogel on the structures, yet clogging still happened in a few cells. If we compare it with the 120s time, the 120s scaffold has more coverage on the beams. Compare it to 150s, hydrogel did not form on the scaffold while 180s seems to be over-polymerized. The fluctuation of hydrogel coverage between each individual scaffold makes it very difficult to conclude a standard time for UV curing.

A possible hypothesis for this fluctuation is that it could be caused by the design of the scaffold, where the I184 photoinitiator did not properly settle everywhere on the scaffold, inside and outside. Additionally, rinsing the samples with IPA directly after the photoinitiator bath could also contribute to the poor settlement of I184 on the scaffolds.

At the point of writing this thesis, a solution have not been found yet for this issue, forming a major obstacle in fully answering the research question.

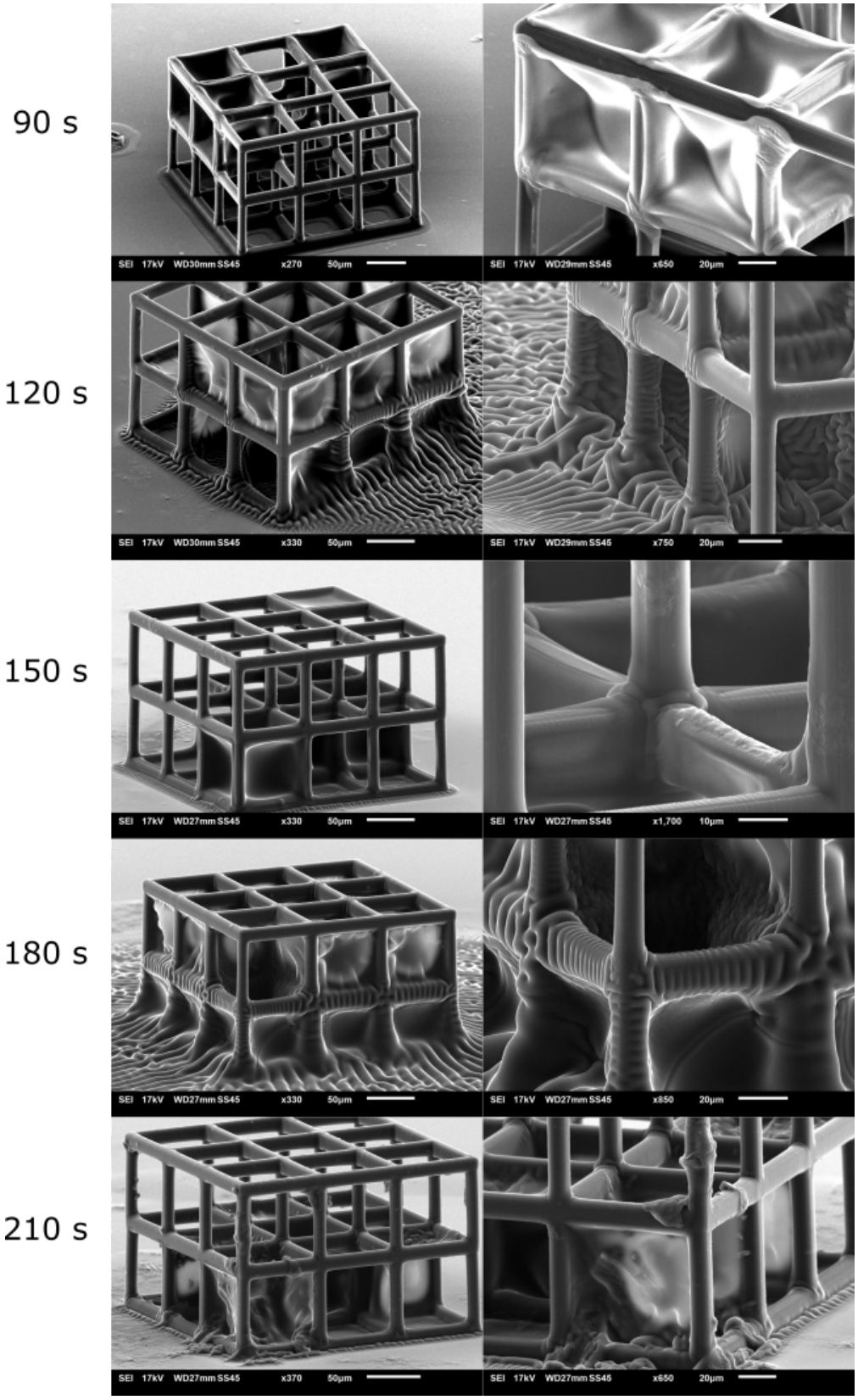

Figure 5.21: A series of SEM images of different lengths of time under UV light, where the high variance of hydrogel growth can be seen.

The last investigated step is a water plunge bath, where the excess hydrogel precursor is washed away. This should be a simple step, but during the thesis it was discovered that the hydrogel skin does not remain attached on the sample. Different plunging time have been tested: 15/30/60 min and 1 night. Displayed in Figure 5.22, it is clear that a water plunging time of 15 minutes still allows the hydrogel to stay on the sample. However, after 30 minutes we already see detachment of the hydrogel. The overnight plunging removed the hydrogel completely. A possible theory is that I184 photoinitiators did not seep into the IP-S polymer properly during the photoinitiator bath.

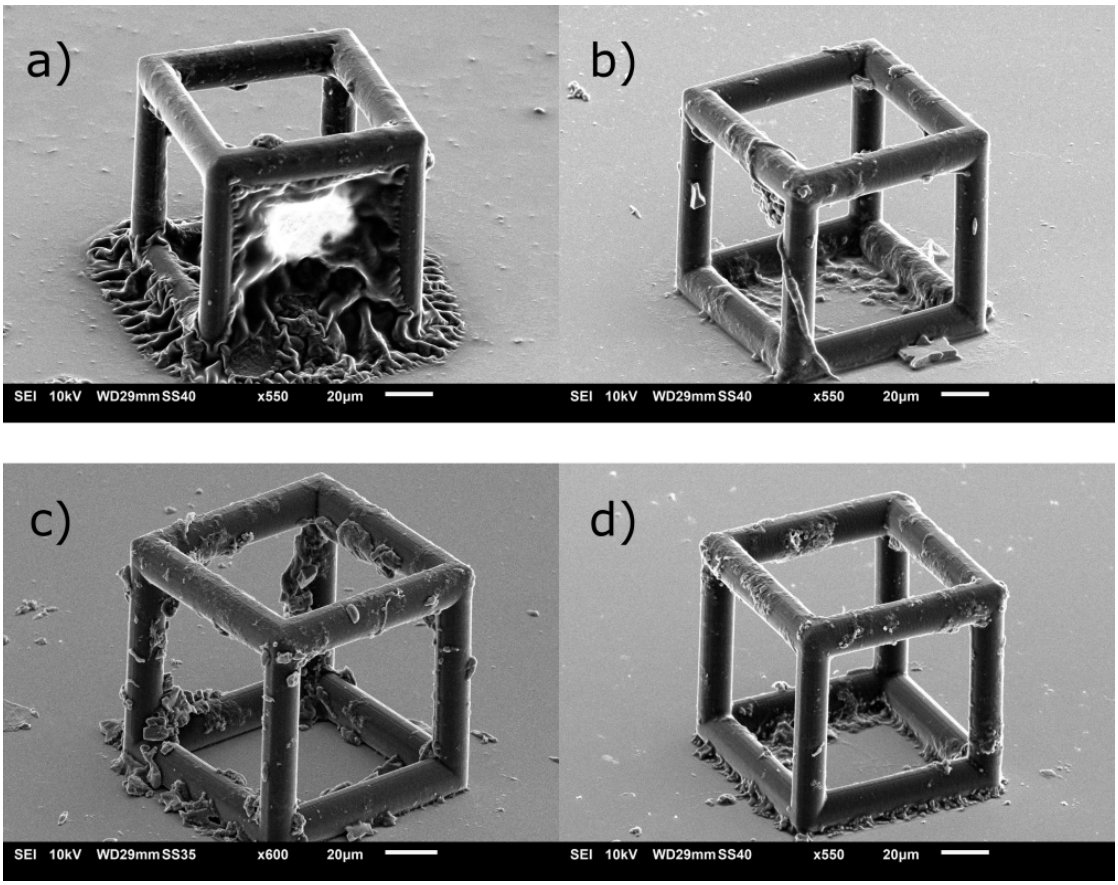

Figure 5.22: Water plunging time test. a) 15 min b) 30 min c) 60 min d) 1 night

Chapter 6
Conclusion

This project was focused on developing a fabrication method to grow soft hydrogel skins on top of 3D micro structures. The fabrication of the 3D structures has a high reproducibility and accuracy. The IP-S polymer is robust and with proper preparations does not delaminate from the substrate. It was shown that soft (430 Pa) hydrogel skins can be grown on a simple pedestal, but not homogeneously on more complex 3D structures. A recurring issue is the forming of hydrogel films clogging the scaffold's pores. Moreover, hydrogel skins did not adhere to the printed structures after plunging in water for more than 15 minutes. The surface-initiated method has a high variance of success rate with larger complex structures. This could be due to the nature of PEGMA monomers, where the long ethylene backbone chain causes the hydrogel films to grow rapidly, thus clogging the pores.

Chapter 7
Future Work and Recommendations

Future work should investigate other hydrogels, because this paper focused on PEGMA, a monomer with long ethylene chains. Possible hydrogels include acrylamide or acrylic acid, which do not contain multiple ethylene backbone. This difference of monomer structure could be the cause for the hydrogel film forming, as PEGMA polymerizes faster than other smaller monomers.

Other possible future work could also focus on a different hydrogel growth technique. This paper focused on a surface-initiated method. During the literature survey, another promising technique was proposed, namely the dip-coating method. This other technique focused on changing the viscosity of the hydrogel precursor and subsequently curing it under UV light. By changing the viscosity of the precursor solution the problem of films may also be solved, as the precursor could just be air dried and evaporate.

More research could be done on combining the surface-initiated method with another IP-resin from the Nanoscribe. The PEGMA hydrogel has been shown to not adhere strongly after plunging in water. An IP-resin that could potentially show more adherence is IP-PDMS, because the initial paper which the surface-initiated method was adapted from used PDMS as one of their substrate.

Chapter 8
Self Reflection

I have enjoyed working on microscale 3D printing and the lab days working on hydrogels in this project even though it was difficult to find results that I am truly satisfied with.

The start of this project was rough as I had no knowledge whether my first results were any good. Working with a broken UV oven also set me back for 2 months while I was still learning the chemistry of hydrogels and free radical polymerization in the lab. I think I should have spent some more time on the chemistry part of this project in order to speed things up.

My weaknesses and challenging parts of this project, which was addressed multiple times, were definitely that I tend to go into details very quickly without context and combined with the fact that I presented my results the same way made it more difficult to communicate my reasonings. I went into this project without a proper understanding of what a true scientific method is, making sometimes baseless claims without support. If there is anything I have understood from this experience is that I need to take into account the people that I am presenting my results to and take a step back. Having an overview of what the results mean in its context would have helped me out much more.

I was very naive for believing that many of my experiments would succeed, as I was very positive and optimistic that my methods would work at the start. Gradually, whenever a set of results did not yield satisfying results, there was still a different combination of parameters that could be tested. In hindsight, I should have gone for more extreme parameters in the beginning to set upper/lower limits of the parameters. I am happy that that is what Ahmed had suggested.

I have also discovered that whenever I encounter an issue, I tend to try to solve it before I move on. For example, I tried to make white light interferometer work with the hydrogel layers I created, but time after time the results were lacking. I was personally really bothered by this because it should work as intended when adding a gold layer. I couldn't move on until I thought of an alternative, which was an AFM. I did not have the knowledge to consider other alternatives back then.

I know that I was just starting in the academic field with this project, but it has really opened up my eyes and revealed my flaws within my methods of working. I am thus thankful for my supervisors who have pointed my flaws out for me and guide me to improve my skills.

Chapter 9

Appendix

A: IP-S properties

Property	Description
Reactive group	methacrylate
Curing mechanism	free radical polymerization (FRP)
Cured Polymer	thermoset
Polarity	hydrophobic

Property	Description
Resin tone	negative
Polymerization	designed for 2PP; UV flood curing is possible
Solution set	3D MF
Fluorescence	yes
Refractive index (liquid)	1.486 @ 589 nm, 20°C
Refractive index (2PP polymerized)	1.515 @ 589 nm, 20°C
Young's modulus	5.11 GPa
Vickers Hardness	20.68 HV0.0025
Hardness	223.33 MPa
Storage modulus	5.33 GPa
Loss modulus	0.26 GPa
Shrinkage after polymerization	2-12%
Density (liquid)	1.111 g/cm³ @ 20°C
Density (solid)	
Swelling	Solvent / Weight increase [%]: purified water 1.5; isopropanol 2; PGMEA 1; acetone 9.5
Viscosity η (liquid)	13600 mPas @ 20°C

Figure 9.1: Properties of IP-S resin

B: EDS spectra

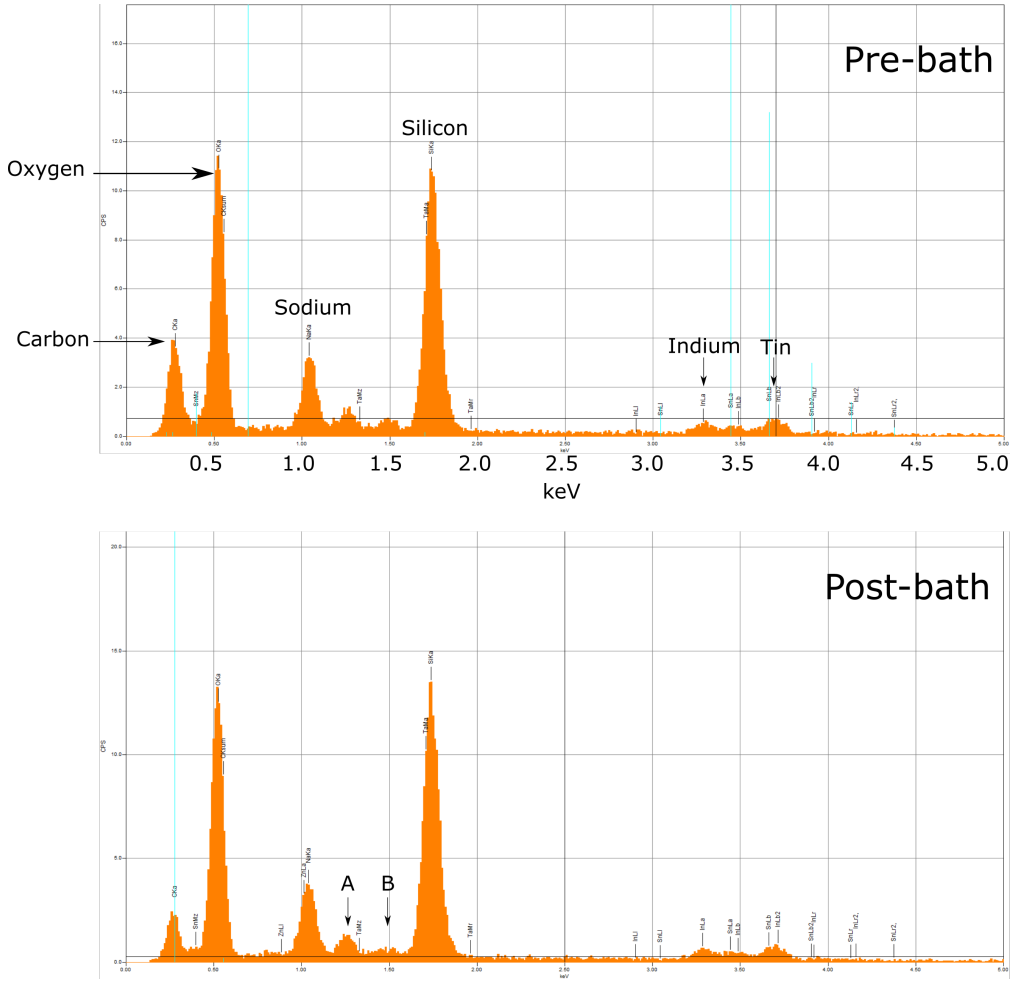

Figure 9.2: EDS spectra pre- and post- photoinitiator bath

C: EDS distribution

Pre-bath

Post-bath

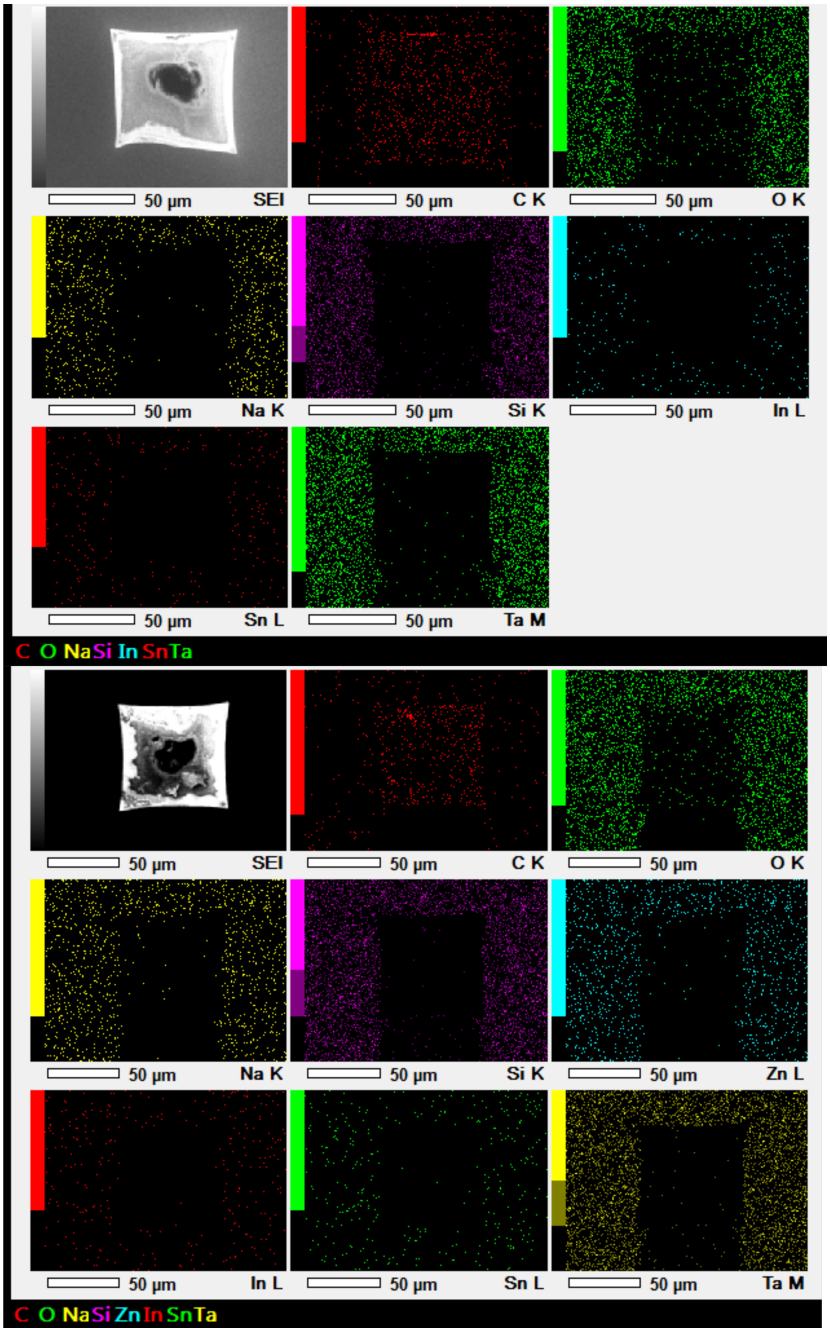

Figure 9.3: Distribution of elements detected pre- and post- I184 initiator bath

D: Raman correlations table

RAMAN Band Correlation Table

Approximate Wavenumber Range (cm–1)	Group	Intensity
100–210	Lattice vibrations	Strong
150–430	Xmetal-O	Strong
250–400	C-C aliphatic chain	Strong
295–340	Se-Se	Strong
425–550	S-S	Strong
460–550	Si-O-Si	Strong
490–660	C-I	Strong
505–700	C-Br	Strong
550–790	C-Cl	Strong
580–680	C=S	Strong
630–1250	C-C aliphatic chains	Moderate
670–780	C-S	Strong
720–800	C-F	Strong
800–950	C-O-C	Weak
910–960	Carboxylic acid dimer	Weak
990–1100	Aromatic rings	Strong
1010–1095	Si-O-C	Weak
1010–1095	Si-O-Si	Weak
1020–1225	C=S	Strong
1025–1060	Sulfonic acid	Very weak
1050–1210	Sulfonamide	Moderate
1050–1210	Sulfone	Moderate
1120–1190	Si-O-C	Weak
1145–1240	Sulfonic acid	Very weak
1315–1435	Carboxylate salt	Moderate
1320–1350	Nitro	Very strong
1355–1385	C-CH3	Weak
1365–1450	Aromatic azo	Very strong
1405–1455	CH2	Weak
1405–1455	CH3	Weak
1450–1505	Aromatic ring	Moderate
1535–1600	Nitro	Moderate
1540–1590	Aliphatic azo	Moderate
1550–1610	Aromatic/hetero ring	Strong
1550–1700	Amide	Strong
1600–1710	Ketone	Moderate
1610–1740	Carboxylic acid	Moderate
1625–1680	C=C	Very strong
1630–1665	C=N	Very strong
1690–1720	Urethane	Moderate
1710–1725	Aldehyde	Moderate
1710–1745	Ester	Moderate
1730–1750	Aliphatic ester	Moderate

Figure 9.4: Raman band correlations table

E: White light interferometer results

White light interferometer data shows big gaps in hydrogel layers, not revealing any information about sample height and therefore no information on hydrogel thickness.

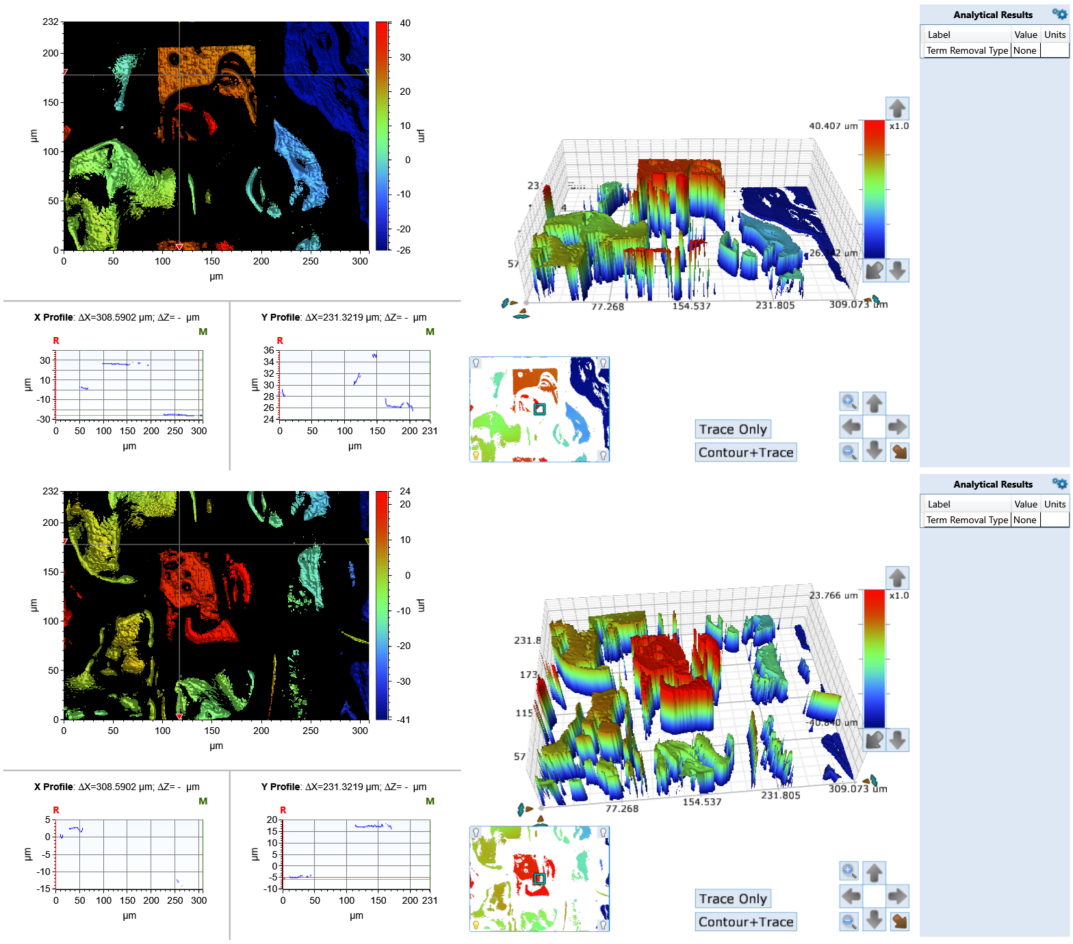

Figure 9.5: White light interferometer results from hydrogel growth on IP-S pedestals

Attempts have been made to improve the visibility of hydrogel. Food dye and gold sputtering on the hydrogel layer did not yield any results.

Bibliography

[1] S. Budday, R. Nay, R. de Rooij, P. Steinmann, T. Wyrobek, T. C. Ovaert, and E. Kuhl, "Mechanical properties of gray and white matter brain tissue by indentation," Journal of the Mechanical Behaviour of Biomedical Materials, vol. 46, pp. 318–330, 2015.

[2] S. Budday, G. Sommer, C. Birkl, C. Langkammer, J. Haybaeck, J. Kohnert, M. Bauer, F. Paulsen, P. Steimann, E. Kuhl, and G. A. Holzapfel, "Mechanical characterization of human brain tissue," Acta Biomaterialia, vol. 48, pp. 319–340, 2017.

[3] C. D. Luca, A. Colangelo, A. Virtuoso, L. Alberghina, and M. Papa, "Neurons, glia, extracellular matrix and neurovascular unit: A systems biology aproach to the complexity of synaptic plasticity in health and disease," International Journal of Molecular Sciences, vol. 21, p. 1539, 2020.

[4] J. W. Haycock, "3D cell culture." `https://link.springer.com/content/pdf/10.1007/978-1-60761-984-0.pdf`, 2011.

[5] DesignerData, "Ps." `https://designerdata.nl/materials/plastics/thermo-plastics/polystyrene`, 2022.

[6] A. materials, "Float glass - properties and applications." `https://www.azom.com/properties.aspx?ArticleID=89`, 2022.

[7] P. Georges, W. Miller, D. Meaney, E. Sawyer, and P. Janmey, "Matrices with compliance comparable to that of brain tissue select neuronal over glial growth in mixed cortical cultures," Biophysical Journal, vol. 90, pp. 3012–3018, 2006.

[8] A. Teixeira, S. Ilkhanizadeh, J. Wigenius, J. Duckworth, O. Inganäs, and O. Hermanson, "The promotion of neuronal maturation on soft substrates," Biomaterials, vol. 30, pp. 4567–4572, 2009.

[9] A. Balgude, X. Yu, A. Szymanski, and R. Bellamkonda, "Agarose gel stiffness determines rate of drg neurite extension in 3d cultures," Biomaterials, vol. 22, pp. 1077–1084, 2001.

[10] M. Kapalczynska, T. Kolenda, W. Przybyla, M. Zajaczkowska, A. Teresiak, V. Filas, M. Ibbs, R. Blizniak, L. Luczewski, and K. Lamperska, "2D and 3D cell cultures - a comparison of different types of cancer cell cultures," Archives of Medical Science, vol. 14, pp. 910–919, 2016.

[11] M. Czerner, L. Fellay, M. Suárez, P. Frontini, and L. Fasce, "Determination of elastic modulus of gelatin gels by indentation experiments," Procedia Materials Science, vol. 8, pp. 287–296, 2015.

[12] J. H. Shepherd, S. Parker, R. Shepherd, M. Gillette, J. Lewis, and R. Nuzzo, "3D microperiodic hydrogel scaffolds for robust neuronal cultures," Advanced Functional Materials, vol. 21, pp. 47–54, 2010.

[13] I. B. an D. Bironaite, E. Bagdonas, and E. Bernotiene, "Scaffolds and cells for tissue regenration: different scaffold pore sizes - different cell effects," Cytotechnology, vol. 68, pp. 355–369, 2015.

[14] A. Ovsianikov, M. Malinauskas, S. Schlie, B. Chichkov, S. Gittard, R. Narayan, M. Löbler, K. Sternberg, K.-P. Schmitz, and A. Haverich, "Three-dimensional laser micro- and nano-structuring of acrylated poly(ethylene glycol) materials and evaluation of their cytoxicity for tissue engineering applications," Acta Biomaterialia, vol. 7, pp. 967–974, 2010.

[15] A. Accardo, M.-C. Blatché, R. Courson, I. Loubinoux, C. Vieu, and L. Malaquin, "Direct laser fabrication of free-standing PEGDA hydrogel scaffolds for neuronal cell growth," Materials Today, vol. 21, 2018.

[16] M. S. Thomsen, L. J. Routhe, and T. Moos, "The vascular basement membrane in the healthy and pathological brain," Journal of Cerebral Blood Flow Metabolism, vol. 37, no. 10, pp. 3300–3317, 2017.

[17] N. K. Karamanos, A. D. Theocharis, Z. Piperigkou, D. Manou, A. Passi, S. S. Skandalis, D. H. Vynios, V. Orian-Rousseau, S. Richard-Blum, C. E. H. Schmelzer, L. Duca, M. Durbeej, N. A. Afratis, L. Troeberg, M. Franchi, V. Masola, and M. Onisto, "A guide to the composition and functions of the extracellular matrix," The FEBS Journal, vol. 288, no. 24, pp. 6850–6912, 2021.

[18] J. Lim and H. Donahue, "Cell sensing and response t omicro- and nanostructured surfaces produced by chemical and topographic patterning," Tissue Engineering, vol. 13, pp. 1879–1891, 2007.

[19] A. Gefen and S. S. Margulies, "Are in vivo and in situ brain tissues mechanically similar?," Journal of Biomechanics, vol. 37, no. 9, pp. 1339–1352, 2004.

[20] M. J. Bissell, "Tissue architecture: the ultimate regulator of breast epithelial function," Current Opinion in Cell Biology, vol. 15, no. 6, pp. 753–762, 2003.

[21] K. A. Kilian, B. Bugarija, B. T. Lahn, and M. Mrksich, "Geometric cues for directing the differentiation of mesenchymal stem cells," Applied Biological Sciences, vol. 107, no. 11, pp. 4872–4877, 2009.

[22] C. M. Nelson and M. J. Bissell, "Of extracellular matrix, scaffolds, and signaling: tissue architecture regulates development, homeostasis, and cancer," Annual Review of Cell and Developmental Biology, vol. 22, pp. 287–309, 2006.

[23] S. Bosi, R. Rauti, J. Laishram, A. Turco, D. Lonardoni, T. Nieus, M. Prato, D. Scaini, and L. Ballerini, "From 2D to 3D: novel nanostructured scaffolds to investigate signalling in reconstructed neuronal networks," Scientific Reports, vol. 5, no. 9562, 2015.

[24] C. Vallejo-Giraldo, M. Genta, O. Cauvi, J. Goding, and R. Green, "Hydrogel for 3D neural tissue models: understanding cell-material interactions at a molecular level," Frontiers in Bioengineering and Biotechnology, vol. 8, 2020.

[25] I. Raimondi, M. Tunesi, G. Forloni, D. Albani, and C. Giordano, "3D brain tissue physiological model with co-cultured primary neurons and glial cells in hydrogels," Journal of Tissue Engineering, vol. 11, no. 2041731420963981, 2020.

[26] M. C. LaPlaca, V. N. Vernekar, J. T. Shoemaker, and D. K. Cullen, "Three-dimensional neuronal cultures," 2007.

[27] Y. Chen, L. Ju, M. Rushdi, C. Ge, and C. Zhu, "Receptor-mediated cell mechanosensing," Molecular Biology of the Cell, vol. 28, pp. 3134–3155, 2017.

[28] C. L. de Rouvroit and A. M. Goffinet, "Neuronal migration," Mechanisms of Development, vol. 105, no. 1, pp. 47–56, 2001.

[29] D. Cojoc, F. Difato, E. Ferrari, R. Shahapure, J. Laishram, M. Righi, E. D. Fabrizio, and V. Torre, "Properties of the force exerted by filopodia and lamellipodia and the involvement of cytoskeletal components," PLOS One, vol. 2, 2007.

[30] D. Koser, A. Thompson, S. Foster, A. Dwivedy, E. Pillai, G. Sheridan, H. Svoboda, M. Viana, L. Costa, J. Guck, C. Holt, and K. Franze, "Mechanosensing is critical for axon growth in the developing brain," Natural Sciences, vol. 19, pp. 1592–1598, 2016.

[31] J. Faix and K. Rottner, "The making of filopodia," Current Opinion in Cell Biology, vol. 18, pp. 18–25, 2006.

[32] K. Leung, F. van Horck, A. Lin, R. Allison, N. Standart, and C. Holt, "Asymmetrical β-actin mRNA translation in growth cones mediates attractive turning to netrin-1," Natuew Neuroscience, vol. 9, pp. 1247–1256, 2007.

[33] K. Jansen, D. Donato, H. Balcioglu, T. Schmidt, and E. Danen, "A guide to mechanobiology: where biology and physics meet," Biochimica et Biophysica Acta (BBA) - Molecular Cell Research, vol. 1853, pp. 3043–3052, 2015.

[34] P. D. Bartlett and F. A. Tate, "The polymerization of allyl compounds. VI. The polymerization of allyl-1-d_2 acetate and the mechanism of its chain termination," Journal of the American Chemical Society, vol. 75, no. 1, pp. 91–95, 1953.

[35] A. Matsumoto, T. Kumagai, H. Aota, H. Kawasaki, and R. Arakawa, "Reassessment of free-radical polymerization mechanism of allyl acetate based on end-group determination of resulting oligomers by MALDI-TOF-MS spectrometry," Polymer Journal, vol. 41, pp. 26–33, 2009.

[36] Z. Wang, A. A. Volinsky, and N. D. Gallant, "Crosslinking effect on polydimethylsiloxane elastic modulus measured by custom-built compression instrument," Journal of Applied Polymer Science, vol. 131, no. 41050, 2014.

[37] D. Fan, U. Staufer, and A. Accardo, "Engineered 3d polymer and hydrogel microenvironments for cell culture applications," Bioengineering, vol. 6, no. 113, 2019.

[38] S. R. Caliari and J. A. Burdick, "A practical guide to hydrogels for cell culture," Nature Methods, vol. 13, pp. 405–414, 2016.

[39] H. Tan, Y. Gong, L. Lao, Z. Mao, and C. Gao, "Gelatin/chitosan/hyaluronan ternary complex scaffold containing basic fibroblast growth factor for cartilage tissue engineering," Journal of Material Science. Materials in Medicine, vol. 10, pp. 1961–1968, 2007.

[40] M. Matyash, F. D. an R. Mandal, D. Fiore, M. Gelinsky, and C. Ikonomidou, "Novel soft alginate hydrogel strongly supports neurite growth and protects neurons against oxidative stress," Tissue Engineering Part A, vol. 18, pp. 55–66, 2011.

[41] J. Chen, Y. Kanai, N. J. Cowan, and N. Hirokawa, "Projection domains of map2 and tau determine spacings between microtubules in dendrites and axons," Nature, vol. 360, pp. 674–677, 1992.

[42] P. F. Moskowitz, R. Smith, J. Pickett, A. Frankfurter, and M. M. Oblinger, "Expression of the class III beta-tubulin gene during axonal regenration of rat dorsal root ganglion neurons," Journal of Neuroscience Research, vol. 34, pp. 129–134, 1993.

[43] H. Chamkouri, "A review of hydrogels, their properties and applications in medicine," American Journal of Biomedical Science & Research, vol. 11, pp. 485–493, 2021.

[44] U. Hersel, C. Dahmen, and H. Kessler, "RGD modified polymers: biomaterials for stimulated cell adhesion and beyond," Biomaterials, vol. 24, pp. 4385–4415, 2003.

[45] J. Ye, S. Fu, S. Zhou, M. Li, K. Li, W. Sun, and Y. Zhai, "Advances in hydrogels based on dynamic covalent bonding and prospects for its biomedical application," European Polymer Journal, vol. 139, no. 110024, 2020.

[46] R. Parhi, "Cross-linked hydrogel for pharmaceutical applications: a review," Advanced Pharmaceutical Bulletin, vol. 7, no. 4, pp. 515–530, 2017.

[47] Y. Wang, W. Zhang, C. Gong, B. Liu, Y. Li, L. Wang, Z. Su, and G. Wei, "Recent advances in the fabrication, functionalization, and bioapplications of peptide hydrogels," Soft Matter, vol. 16, pp. 10029–10045, 2020.

[48] X. Yao, Y. Liu, C. Yang, X. Yang, J. Wei, Y. Xia, X. Gong, and Z. Suo, "Hydrogel paint," Advanced Materials, vol. 31, 2019.

[49] Y. Yu, H. Yuk, G. A. Parada, Y. Wu, X. Liu, C. S. Nabzdyk, K. Youcef-Toumi, J. Zang, and X. Zhao, "Multifunctional "hydrogel skins" on diverse polymers with arbitrary shapes," Advanced Materials, vol. 31, no. 7, p. 1807101, 2019.

[50] S. Wang, Z. Wang, J. Li, L. Li, and W. Hu, "Surface-grafting polymers: frmo chem-

istry to organic electronics," Materials Chemistry Frontiers, vol. 4, no. 3, pp. 692–714, 2020.

[51] F. Klein, T. Striebel, J. Fischer, Z. Jiang, C. M. Franz, G. von Freymann, M. Wegener, and M. Bastmeyer, "Elastic fully three-dimensional microstructurescaffolds for cell force measurements," Advanced Materials, vol. 22, pp. 868–871, 2010.

[52] J. K. Hohmann and G. von Freymann, "Influence of direct laser written 3d topographies on proliferation and differentiation of osteoblast-like cells: Towards improved implant surfaces," Advanced Functional Materials, vol. 24, no. 42, pp. 6573–6580, 2014.

[53] G. P. Dillon, X. Yu, A. Sridharan, and J. P. R. ad R. V. Bellamkonda, "The influence of physical structure and charge on neurite extension in a 3D hydrogel scaffold," Journal of Biomaterials Science: Polymer Edition, vol. 9, pp. 1049–1069, 1998.

[54] Z. F. Rad, P. D. Prewett, and G. J. Davies, "High-resolution two-photon polymerization: the most verstaile technique for the fabrication of microneedle arrays.," Microsystems Nanoengineering, vol. 7, no. 71, 2021.

[55] T. A. Otitju, A. L. Ahmad, and B. S. Ooi, "Superhydrophilic (superwetting) surfaces: A review on fabrication and application," Journal of Industrial and Engineering Chemistry, vol. 47, pp. 19–40, 2017.

[56] B. Majhy, R. Iqbal, and A. K. Sen, "Facile fabrication and mechanistic understanding of a transparent reversible superhydrophobic – superhydrophilic surface," Scientific Reports, vol. 8, no. 18018, 2018.

[57] M. Vuckovac, M. Latikka, K. Liu, T. Huhtamäki, and R. H. A. Ras, "Uncertainties in contact angle goniometry," Soft Matter, vol. 15, pp. 7089–7096, 2019.

[58] A. K. Bansal, S. Patel, and A. M. Kaushal, "Effect of starch paste and sodium starch glycolate on compaction behavior of wet granulated paracetamol formulations studied using a fully instrumented rotary tablet press," Journal of Excipients and Food Chemicals, vol. 2, pp. 64–72, 2011.

[59] X. Liu, R. Fernandes, A. Jurisicova, R. F. Casper, and Y. Sun, "In situ mechanical characterization of mouse oocytes using a cell holding device," Lab on a Chip, vol. 10, no. 16, pp. 2154–2161, 2010.

[60] M. Student, "What is scanning electron microscopy? (how it works, applications, and limitations)." `https://msestudent.com/what-is-scanning-electron-microscopy-how-it-works-applications-and-limitations/`.

[61] E. Instruments, "What is raman spectroscopy?," 2022.